







## Article

# Efficient and Stable Air-Processed Ternary Organic Solar Cells Incorporating Gallium-Porphyrin as an Electron Cascade Material

Anastasia Soultati <sup>1</sup>, Maria Verouti <sup>1,2</sup>, Ermioni Polydorou <sup>1</sup>, Konstantina-Kalliopi Armadorou <sup>1</sup>, Zoi Georgiopoulou <sup>1,3</sup>, Leonidas C. Palilis <sup>2</sup>, Ioannis Karatasios <sup>1</sup>, Vassilis Kilikoglou <sup>1</sup>, Alexander Chroneos <sup>4,5</sup>, Athanassios G. Coutsolelos <sup>6,\*</sup>, Panagiotis Argitis <sup>1,\*</sup> and Maria Vasilopoulou <sup>1,\*</sup>

- <sup>1</sup> Institute of Nanoscience and Nanotechnology (INN), National Center for Scientific Research Demokritos, Agia Paraskevi, 15341 Athens, Greece; a.soultati@inn.demokritos.gr (A.S.); marwver@gmail.com (M.V.); e.polydorou@inn.demokritos.gr (E.P.); karmadorou@gmail.com (K.-K.A.); zoegeorgiopoulou@gmail.com (Z.G.); i.karatasios@inn.demokritos.gr (I.K.); v.kilikoglou@inn.demokritos.gr (V.K.)
- <sup>2</sup> Department of Physics, University of Patras, 26504 Rio Patra, Greece; lpalilis@upatras.gr
- <sup>3</sup> Solid State Physics Section, Physics Department, National and Kapodistrian University of Athens, Panepistimioupolis, 15784 Athens, Greece
- <sup>4</sup> Department of Electrical and Computer Engineering, University of Thessaly, 38221 Volos, Greece; alexander.chroneos@imperial.ac.uk
- <sup>5</sup> Department of Materials, Imperial College, London SW7 2AZ, UK
- <sup>6</sup> Laboratory of Bioinorganic Chemistry, Department of Chemistry, University of Crete, Voutes Campus, P.O. Box 2208, 71003 Heraklion, Greece
- \* Correspondence: acoutsol@uoc.gr (A.G.C.); p.argitis@inn.demokritos.gr (P.A.); m.vasilopoulou@inn.demokritos.gr (M.V.)



**Citation:** Soultati, A.; Verouti, M.; Polydorou, E.; Armadorou, K.-K.; Georgiopoulou, Z.; Palilis, L.C.; Karatasios, I.; Kilikoglou, V.; Chroneos, A.; Coutsolelos, A.G.; et al. Efficient and Stable Air-Processed Ternary Organic Solar Cells Incorporating Gallium-Porphyrin as an Electron Cascade Material. *Nanomaterials* **2023**, *13*, 2800. <https://doi.org/10.3390/nano13202800>

Academic Editors: Rodrigo Martins, Hugo Aguas and Zhan'ao Tan

Received: 8 September 2023  
Revised: 12 October 2023  
Accepted: 19 October 2023  
Published: 21 October 2023



**Copyright:** © 2023 by the authors. Licensee MDPI, Basel, Switzerland. This article is an open access article distributed under the terms and conditions of the Creative Commons Attribution (CC BY) license (<https://creativecommons.org/licenses/by/4.0/>).

**Abstract:** Two gallium porphyrins, a tetraphenyl GaCl porphyrin, termed as (TPP)GaCl, and an octaethylporphyrin GaCl porphyrin, termed as (OEP)GaCl, were synthesized to use as an electron cascade in ternary organic bulk heterojunction films. A perfect matching of both gallium porphyrins' energy levels with that of poly(3-hexylthiophene-2,5-diyl) (P3HT) or poly[N-9'-heptadecanyl-2,7-carbazole-alt-5,5-(4',7'-di-2-thienyl-2',1',3'-benzothiadiazole)] (PCDTBT) polymer donor and the 6,6-phenyl C<sub>71</sub> butyric acid methyl ester (PCBM) fullerene acceptor, forming an efficient cascade system that could facilitate electron transfer between donor and acceptor, was demonstrated. Therefore, ternary organic solar cells (OSCs) using the two porphyrins in various concentrations were fabricated where a performance enhancement was obtained. In particular, (TPP)GaCl-based ternary OSCs of low concentration (1:0.05 vv%) exhibited a ~17% increase in the power conversion efficiency (PCE) compared with the binary device due to improved exciton dissociation, electron transport and reduced recombination. On the other hand, ternary OSCs with a high concentration of (TPP)GaCl (1:0.1 vv%) and (OEP)GaCl (1:0.05 and 1:0.1 vv%) showed the poorest efficiencies due to very rough nanomorphology and suppressed crystallinity of ternary films when the GaCl porphyrin was introduced to the blend, as revealed from X-ray diffraction (XRD) and atomic force microscopy (AFM). The best performing devices also exhibited improved photostability when exposed to sunlight illumination for a period of 8 h than the binary OSCs, attributed to the suppressed photodegradation of the ternary (TPP)GaCl 1:0.05-based photoactive film.

**Keywords:** gallium porphyrin; electron cascade; ternary organic solar cell; exciton dissociation efficiency; photostability

## 1. Introduction

Today's energy crisis has caused a shock of unprecedented breadth and intricacy, leading to the evaluation of renewable energy opportunities that meet the continuous

electricity demand. Hence, exploiting solar energy for power generation has become even more imperative nowadays, shaping the photovoltaic research landscape [1–6]. Given the significance of briskly diversifying our energy supply and enhancing energy efficiency, overcoming the hurdles concerning global organic solar cell (OSC) promotion should be a priority for all interested parties involved, from academics and publishers to companies and funding agencies. Among different photovoltaic technologies, OSCs are thin-film solar cells with unique features for either outdoor [7–9] or indoor use [10–14]. The possibility of their application for large area coverage [15–18], their semitransparent character [19–21], and their low-cost fabrication by printing methods [18,22–24], enable OSCs to be integrated into buildings' facades and windows or sunroofs. In this way, OSCs can provide energy derived from sunlight that might either warm a room or contribute to electric power (i.e., hybrid vehicles). [25–28]. Furthermore, due to their lightweight nature [29,30], flexibility [31,32] and coloration [33], OSCs can be an affordable solution for delivering smaller quantities of electricity required for wearable [34–36] and portable electronics [37]. On the other hand, indoor OSCs appear to have great application potential in the Internet of Things [38,39] and energy harvesting [40,41].

OSCs could also play a crucial role in the reduction of electronic waste, known as e-waste, which is rapidly accelerating in our modern way of life [42]. The annual production of e-waste is globally estimated to be over 50 million tons; therefore, green and sustainable technologies are urgent. Not only low-toxic organic materials and solvents, but also recycling substrates have been used for the fabrication of OSCs [43,44]. Zhou et al. [45] demonstrated the first efficient and recyclable organic solar cell on cellulose nanocrystal substrates. The separation of the fabricated OSCs into their major components with low-energy and low-temperature processing paved the way for a fully recyclable, sustainable and eco-friendly solar cell technology.

Undoubtedly, OSCs provide the momentum for a large number of technological applications. In recent years, sustained research efforts have notably increased the solar-to-electrical power conversion efficiencies of OSCs to a satisfying level for them to be brought to market. The most efficient semitransparent OSC yielded a power conversion efficiency (PCE) of 19% [46], while a record high efficiency of 28% for indoor OSC has also been reported [47]. Nevertheless, despite the fact that OSCs have reached the performance of their predecessors, unfortunately their commercialization is restricted by stability issues. Instability in OSCs is dictated by a series of degradation modes that are usually assigned to the stability of individual materials or interfaces [48–51]. For instance, many organic compounds are chemically degraded when constantly irradiated, mainly owing to their susceptibility to atmospheric oxygen [52] and moisture [53]. Additionally, morphological degradation may occur under extreme environmental conditions, such as extended light exposure and elevated temperatures. Climate variability that meets outdoor operation can lead to the diffusion of buffer layers and electrodes, and especially to the evolution of the phase-segregated bulk-heterojunction (BHJ) active layer due to the strong mobility of organic materials, stressing the cell and eventually causing its decaying performance [48,54].

It is well-known that ideal active layer morphology, aside from having a favorable molecular orientation to optimize charge transport and being compositionally structured in vertical direction to facilitate charge collection, should simultaneously form a bicontinuous network of mixed nanodomains of semiconducting materials for efficient exciton dissociation and suppression of charge recombination [55–59]. Accordingly, the morphology of active layers plays a pivotal role in impacting the overall photovoltaic performance. While many strategies, including material optimization [60,61], device engineering [62] and encapsulation processes [63], have been proposed to improve and stabilize active layer morphology, structural engineering is identified as a strategic priority. In this context, numerous reports have emerged that focus on designing effective additives to enhance the electronic and/or morphological properties of typical OSC systems with the commonly used poly(3-hexylthiophene) (P3HT) and phenyl-C<sub>61</sub>-butyric acid methyl ester (PC<sub>61</sub>BM) as donor and acceptor, respectively [64–67].

The approach of adding a third component to form ternary BHJ blends for solar cells entails some specific intermolecular interactions in terms of controlling morphology. The third component should also act as a cascade layer reducing the charge transfer energy offsets at the donor/acceptor lowest unoccupied molecular orbital (LUMO) levels, resulting in reduced recombination losses. In addition, the cascade material should have excellent electron acceptor and transport properties for the case of the formation of a heterojunction between the third component and the donor polymer. In this vein, porphyrins appear to be suitable candidates as components that could be functional BHJ additives. Owing to their strong absorption properties (high extinction coefficients) in both the blue (~400–550 nm, Soret or B-band) and red (~700–900 nm, Q-band) regions of the visible spectrum, their high thermal stability and their remarkable electron transfer capability, porphyrins have been successfully applied in organic and planar perovskite solar cells as cathode interfacial modifiers, realizing efficient device operation and longevity [68,69]. Following this thinking, porphyrins could be introduced as a cascade energy material in a binary BHJ blend inducing efficient charge extraction as they can provide more efficient charge transport pathways [70]. Herein, we demonstrate the effect of two gallium porphyrins, tetraphenyl GaCl porphyrin, termed as (TPP)GaCl, and an octaethylporphyrin GaCl porphyrin, termed as (OEP)GaCl, in various ratios, as additives in two different binary photoactive blends. The organic blends consist of poly(3-hexylthiophene-2,5-diyl) (P3HT) or poly[N-9'-heptadecanyl-2,7-carbazole-alt-5,5-(4',7'-di-2-thienyl-2',1',3'-benzothiadiazole)] (PCDTBT) polymer donors with the 6,6-phenyl C<sub>71</sub> butyric acid methyl ester (PCBM) fullerene acceptor. In this study, the photophysical properties of the target porphyrins, alone and within the binary host BHJ blends, were studied by means of optical spectroscopy, while Fourier-transform infrared (FTIR) spectroscopy was used to analyze the chemical composition in every case and the possible interaction between the three components of the ternary films. Additionally, electrochemical characterization of the porphyrin compounds was performed to estimate the highest occupied molecular orbital (HOMO) and lowest unoccupied molecular orbital (LUMO) levels of the two porphyrins, revealing the potential role of GaCl porphyrins as electron cascade materials. Therefore, ternary organic solar cells using both porphyrins as the third component inserted in the PCDTBT:PCBM or P3HT:PCBM binary blend in various concentrations were fabricated. Note that all ternary and binary OSCs were prepared in air (without using glove box), at room temperature (25°) and under 40% humidity (without using glove box) to promote a low-cost fabrication procedure. The addition of (TPP)GaCl with low concentrations (1:0.05 vv%, see Section 4 for more details) increased the PCE of the ternary OSCs by ~17% in comparison with the efficiency of the binary devices, which were assigned to the enhanced electron transport and exciton dissociation into free charges, along with the reduced recombination. On the other hand, when (TPP)GaCl with higher concentrations or (OEP)GaCl was added to the ternary film, a rougher morphology surface and suppressed crystallinity were observed leading to poor PCE values of the corresponding ternary OSCs. The ternary (TPP)GaCl 1:0.05 vv%-based OSC also exhibited enhanced photostability under exposure to sunlight illumination for a period of 8 h, attributed to the better structural stability of the ternary films than the binary layer.

## 2. Results and Discussion

### 2.1. Characterization of (TPP)GaCl and (OEP)GaCl Porphyrin Materials

Two gallium porphyrin materials, a tetraphenyl GaCl porphyrin, termed as (TPP)GaCl, and an octaethylporphyrin GaCl porphyrin, termed as (OEP)GaCl, were synthesized following a previous procedure [71] to use as the third component in ternary organic BHJ films. In brief, to a solution of porphyrin (1.9 mmol) and GaCl (9 mmol) in 100 mL of acetic acid, sodium acetate (25 mmol) was added in 200 mL of acetic acid. The mixture was refluxed for 24 h, and, after returning to ambient temperature, the solid precipitate was collected, dried and recrystallized in a toluene–heptane mixture. Prior to the incorporation of the porphyrins as a third component in the binary blends P3HT:PCBM and PCDTBT:PCBM,

their optical and electrochemical properties were investigated. It should be mentioned that these molecules were selected due to their fine solubility in the same organic solvent of the organic blends [72]. The molecular structure of the gallium porphyrins, which constitute four phenyl ( $C_6H_5$ ) groups attached to the pyrrole rings [71], are shown in Figure 1a, and their Fourier-transform infrared and UV-Vis absorption spectra are displayed in Figure 1b,c, respectively.

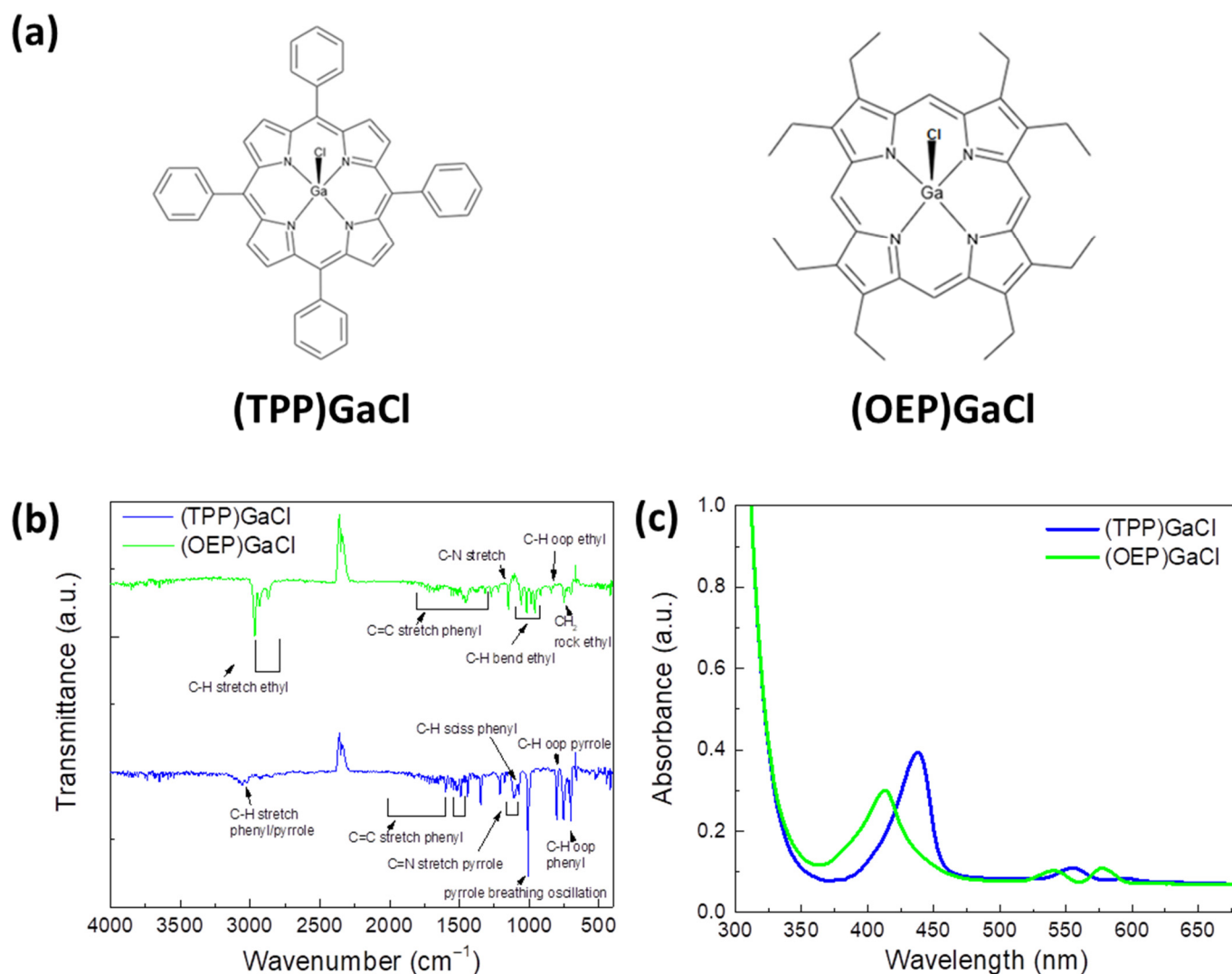


**Figure 1.** (a) Molecular structure of (TPP)GaCl and (OEP)GaCl porphyrins. (b) FTIR transmittance and (c) UV-Vis absorption spectra of the corresponding porphyrin thin films.

In the FTIR transmittance spectrum of the (TPP)GaCl, weak peaks at around  $3050\text{ cm}^{-1}$  corresponding to the C-H stretching vibrations of aromatic groups are observed. Moreover, peaks at  $1107\text{ cm}^{-1}$  and  $802\text{ cm}^{-1}$  are attributed to the C-H scissoring of phenyl rings in and out of the plane bending mode of the pyrrole rings, respectively, while peaks at  $701\text{ cm}^{-1}$  and  $754\text{ cm}^{-1}$  are assigned to the out-of-plane bending of the phenyl rings. In the area from  $1347\text{ cm}^{-1}$  to  $1600\text{ cm}^{-1}$ , multiple peaks corresponding to the stretching vibration of the C=C aromatic groups of phenyl are observed, while in the  $1175\text{--}1206\text{ cm}^{-1}$  region the stretching mode of C=N in pyrrole rings appears. The peak of the Ga-Cl bond is not observed in the spectrum, since it can be found in the region  $330\text{--}370\text{ cm}^{-1}$  [73], which is out of the range of our FTIR instrument. On the other hand, in the FTIR spectrum of (OEP)GaCl, the C=C stretching mode of the phenyl rings and the C-N stretching mode of the pyrrole groups are detected at the  $1300\text{--}1580\text{ cm}^{-1}$  region and at  $1150\text{ cm}^{-1}$ , respectively. The

bands ascribed to the substitution of the pyrrole unit correspond to the vibration modes of the ethyl group. Specifically, those peaks are found at  $2966\text{ cm}^{-1}$ ,  $2930\text{ cm}^{-1}$  and  $2869\text{ cm}^{-1}$  (C-H stretching), in the  $960\text{--}1160\text{ cm}^{-1}$  region (C-H bending), at  $842\text{ cm}^{-1}$  (C-H out-of-plane bending) and at  $749\text{ cm}^{-1}$  (rocking mode of  $\text{CH}_2$  group).

Figure 1c shows the UV-Vis absorption spectra of both porphyrins spin-coated on a glass from a chloroform solution with a concentration of  $1\text{ mg mL}^{-1}$ . It is observed that both gallium porphyrins exhibit typical Soret bands in the range of  $375\text{--}475\text{ nm}$ , and the Q-bands are all located at  $515\text{--}625\text{ nm}$  revealing further electronic transitions in the molecular orbitals. In particular, the (TPP)GaCl porphyrin exhibits a sharper Soret band centered at  $438\text{ nm}$  and two weak Q bands at  $555$  and  $595\text{ nm}$ , while the (OEP)GaCl porphyrin has a broader Soret band located at  $413\text{ nm}$  and two Q bands at  $541$  and  $577\text{ nm}$ .

In order to examine the possible use of these porphyrin compounds as electron cascades in BHJ blends, their energy levels ( $E_{\text{HOMO}}$  and  $E_{\text{LUMO}}$ ) were estimated by performing cyclic voltammetry. Figure 2a–d shows the cyclic voltammograms of (TPP)GaCl and (OEP)GaCl porphyrins deposited on indium tin oxide (ITO)/glass substrates. Oxidation and reduction potentials are summarized in Table 1 together with the estimation of the corresponding HOMO and LUMO levels evaluated by using the following empirical formulas [74]:

$$E_{\text{HOMO}} = -(E_{|\text{onset,oxvsF}_c^+/\text{Fc}|} + 5.1) \text{ (eV)} \quad (1)$$

$$E_{\text{LUMO}} = -(E_{|\text{onset,redvsF}_c^+/\text{Fc}|} + 5.1) \text{ (eV)} \quad (2)$$

where  $E_{|\text{onset,oxvsF}_c^+/\text{Fc}|}$  and  $E_{|\text{onset,redvsF}_c^+/\text{Fc}|}$  are the oxidation and reduction potential onsets in respect to ferrocene, respectively, defined as the position where the current starts to differ from the baseline. From the cyclic voltammograms the  $E_{|\text{onset,oxvsF}_c^+/\text{Fc}|}$  value is  $+0.5\text{ V}$  and  $+0.4\text{ V}$  for (TTP)GaCl and (OEP)GaCl, respectively, which results in HOMO levels of  $-5.6\text{ eV}$  for (TTP)GaCl and  $-5.5\text{ eV}$  for (OEP)GaCl. The LUMO levels of (TTP)GaCl and (OEP)GaCl are  $-3.8\text{ eV}$  and  $-3.9\text{ eV}$ , respectively, and are determined by the reduction potential onset ( $-1.3\text{ V}$  for (TTP)GaCl and  $-1.2\text{ V}$  for (OEP)GaCl). The energy diagram illustrated in Figure 2e reveals the perfect matching of both gallium porphyrins' energy levels with that of the polymer donors (PCDTBT or P3HT) and the PCBM acceptor, forming an efficient cascade system that could facilitate electron transfer between donor and acceptor.

**Table 1.** Cyclic voltammetry calculated data of porphyrins.

Porphyrin	$E_{\text{ox}}$ (eV)	$E_{\text{red}}$ (eV)	$E_{\text{HOMO}}$	$E_{\text{LUMO}}$
(TTP)GaCl	0.5	$-1.3$	$-5.6$	$-3.8$
(OEP)GaCl	0.4	$-1.2$	$-5.5$	$-3.9$

## 2.2. Characterization of Ternary Blend Films

Figure 3a,b and Figure S1a,b presents the UV-Vis absorption spectra of ternary PCDTBT:PCBM:Ga-porphyrin and P3HT:PCBM:Ga-porphyrin films, respectively, forming on a glass substrate from a chloroform solution, as described in the Section 4. The binary PCDTBT:PCBM and P3HT:PCBM are also shown for comparison reasons. UV-Vis absorption spectra of the PCDTBT:PCBM film display a peak centered at  $381\text{ nm}$  and a broad absorption band from  $500\text{ nm}$  to  $640\text{ nm}$  (Figure 3a,b), while the P3HT:PCBM spectrum exhibits three absorption regions of P3HT at  $501\text{ nm}$ ,  $545\text{ nm}$  and  $597\text{ nm}$ , and extends into the visible region from approximately  $400\text{ nm}$  to  $700\text{ nm}$  (Figure S1a,b). In the spectra of the ternary films, the peak corresponding to the Soret band of both porphyrin compounds is clearly seen. Moreover, the blue shift of the PCDTBT:PCBM and P3HT:PCBM spectra is observed when (TTP)GaCl and (OEP)GaCl porphyrins are incorporated into binary blends, which is more pronounced in the case of the (OEP)GaCl-based ternary films, and especially in the P3HT:PCBM:GaCl.

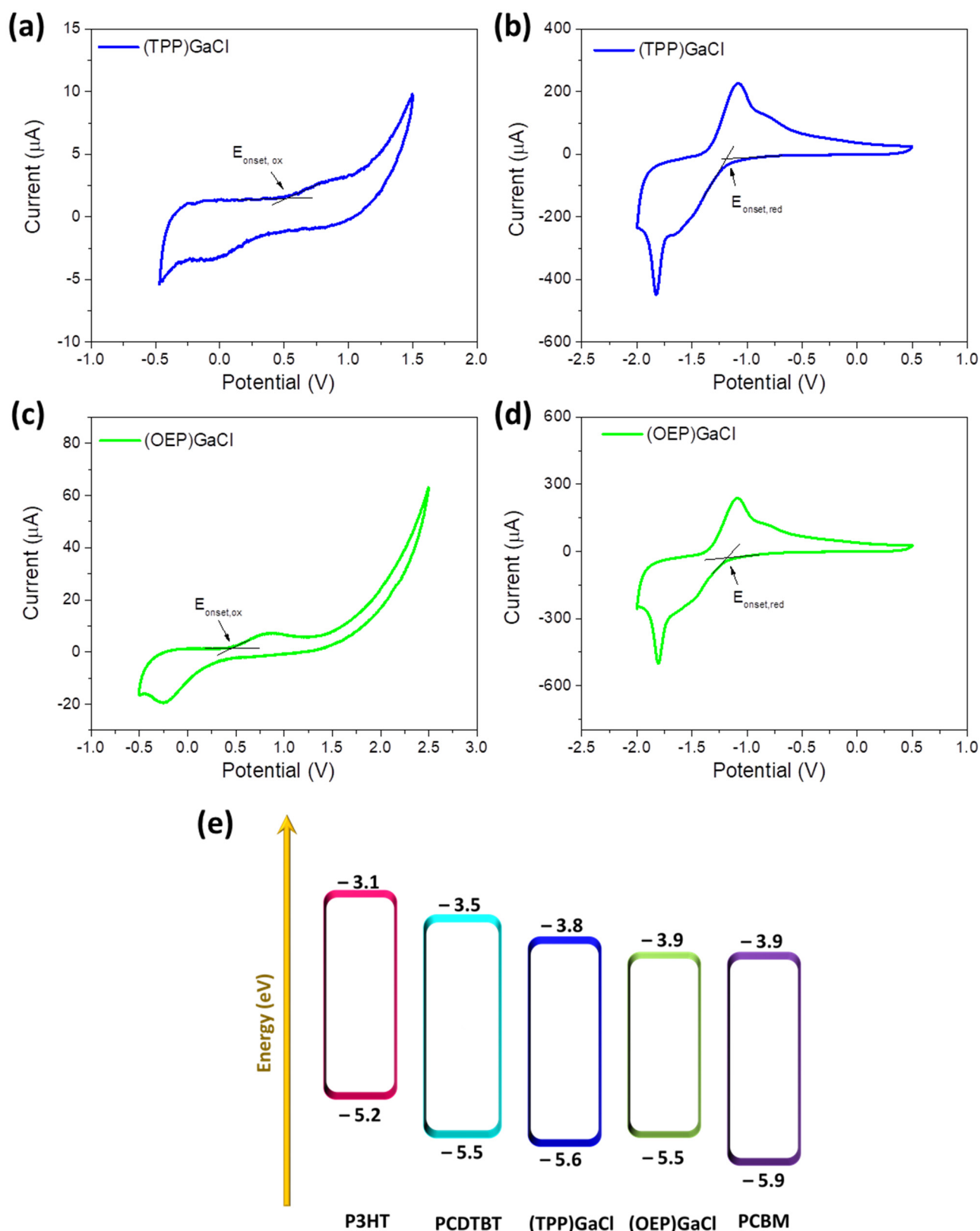


**Figure 2.** Cyclic voltammograms of (a,b) (TPP)GaCl and (c,d) (OEP)GaCl porphyrins. (a,c) refers to the oxidation processes, while (b,d) to the reduction processes. (e) Schematic energy level diagram of the organic semiconductors and gallium–porphyrin compounds illustrating the functionalization of porphyrins as electron cascade.

In order to investigate the chemical structure of the prepared ternary films, FTIR transmittance measurements were performed. In the FTIR spectra of PCDTBT:PCBM:(TPP):GaCl, shown in Figure 3c, a combination of peaks attributed to all three components of the ternary film are observed. In particular, the peaks at  $2925\text{ cm}^{-1}$ ,  $2852\text{ cm}^{-1}$  (C-H stretch), at  $1739\text{ cm}^{-1}$  (C=O stretch), at  $1494\text{ cm}^{-1}$  (C=C stretch), in the region  $1330\text{--}1430\text{ cm}^{-1}$  ( $\text{CH}_2$  and  $\text{CH}_3$  bend), at  $1250\text{ cm}^{-1}$  (C-O stretch) and at  $1106\text{ cm}^{-1}$  (C-O bend) are assigned to the binary PCDTBT:PCBM blend. The only apparent (TPP)GaCl absorption band in the ternary film is detected in the aromatic stretching region, which can be seen in the spectrum of the sample with a 1:0.1 vv% ratio. In addition, the pyrrole breathing oscillation peak is detected at  $1007\text{ cm}^{-1}$ . In addition, some weak peaks under  $1000\text{ cm}^{-1}$ , corresponding to the porphyrins, are apparent ( $802$ ,  $754$  and  $701\text{ cm}^{-1}$ ). On the other hand, the porphyrin peaks located at  $3050\text{ cm}^{-1}$  in the  $1175\text{--}1206\text{ cm}^{-1}$  region and in the  $1107\text{--}1110\text{ cm}^{-1}$  region cannot be observed in the ternary film, due to the low concentration of the (TPP)GaCl porphyrin with respect to the binary blend. Similarly, in the case of PCDTBT:PCBM:(OEP)GaCl (Figure 3d), the C-H stretching peaks just below  $3000\text{ cm}^{-1}$ , located at  $2966$ ,  $2925$  and  $2852\text{ cm}^{-1}$ , are a combination of the peaks from the binary blend and the porphyrin additive corresponding to the same vibration mode. The carbonyl peak at  $1739\text{ cm}^{-1}$  remains unchanged, while the C=C stretching peaks of the porphyrin overlap with all other polymer blend peaks found in the region, more specifically at  $1494\text{ cm}^{-1}$  (C=C stretch),  $1430\text{--}1330\text{ cm}^{-1}$  ( $\text{CH}_2$  and  $\text{CH}_3$  bend) and  $1250\text{ cm}^{-1}$  (C-O stretch). Just below this region, the C-O bending peak at  $1106\text{ cm}^{-1}$  can be seen, while the C-N stretching peak of the porphyrin is absent from the ternary film. Furthermore, porphyrin weak peaks at  $1160\text{--}960\text{ cm}^{-1}$  (C-H bend ethyl) are depicted. The same results can be also concluded for the ternary P3HT:PCBM:(TPP)GaCl and P3HT:PCBM:(OEP)GaCl ternary films, the FTIR transmittance spectra of which are shown in Figures S1c and S1d, respectively.

Moreover, photoluminescence (PL) measurements were applied to probe the efficiency of the exciton dissociation and charge transfer. Figures 3e,f and S1e,f illustrate the photoluminescence steady-state emission (PL) spectra of various samples, including pristine films and blends of PCDTBT and P3HT with (TPP)GaCl and (OEP)GaCl in ratios of 1:0.05 and 1:0.1. In the PL spectrum of the pure P3HT film, a peak corresponding to excitonic emission is observed at  $653\text{ nm}$  (Figure S1e). Upon introducing (TPP)GaCl to the P3HT blend, the PL intensity decreases, indicating that efficient charge transfer occurred from P3HT and (TPP)GaCl. On the other hand, the addition of (OEP)GaCl results in increased fluorescence of P3HT, potentially attributable to the aggregation of (OEP)GaCl molecules. The well-known tendency of porphyrin molecules to aggregate could form plasmonic nanostructures in the ternary blends. Plasmonic effects through metal nanostructures enhance photon absorption and charge transfer leading to an improved photocurrent due to hot electron generation in the metal nanostructure [75,76]. Plasmon formation using GaCl-based porphyrin molecules is currently being investigated and the corresponding results will be demonstrated in a subsequent work. Additionally, a shift towards longer wavelengths (redshift) is noted in the PL spectrum of P3HT, particularly at higher concentrations of (OEP)GaCl. This shift may be ascribed to the presence of trapped states within the energy gap of (OEP)GaCl, aligning with the lowest energy states in the highest occupied molecular orbital (HOMO) of P3HT. Consequently, notable recombination occurs between photoinduced holes originating from the lowest HOMO states of P3HT and deep traps of (OEP)GaCl, along with enhanced photoinduced electron back transfer from the LUMO to the HOMO of P3HT.

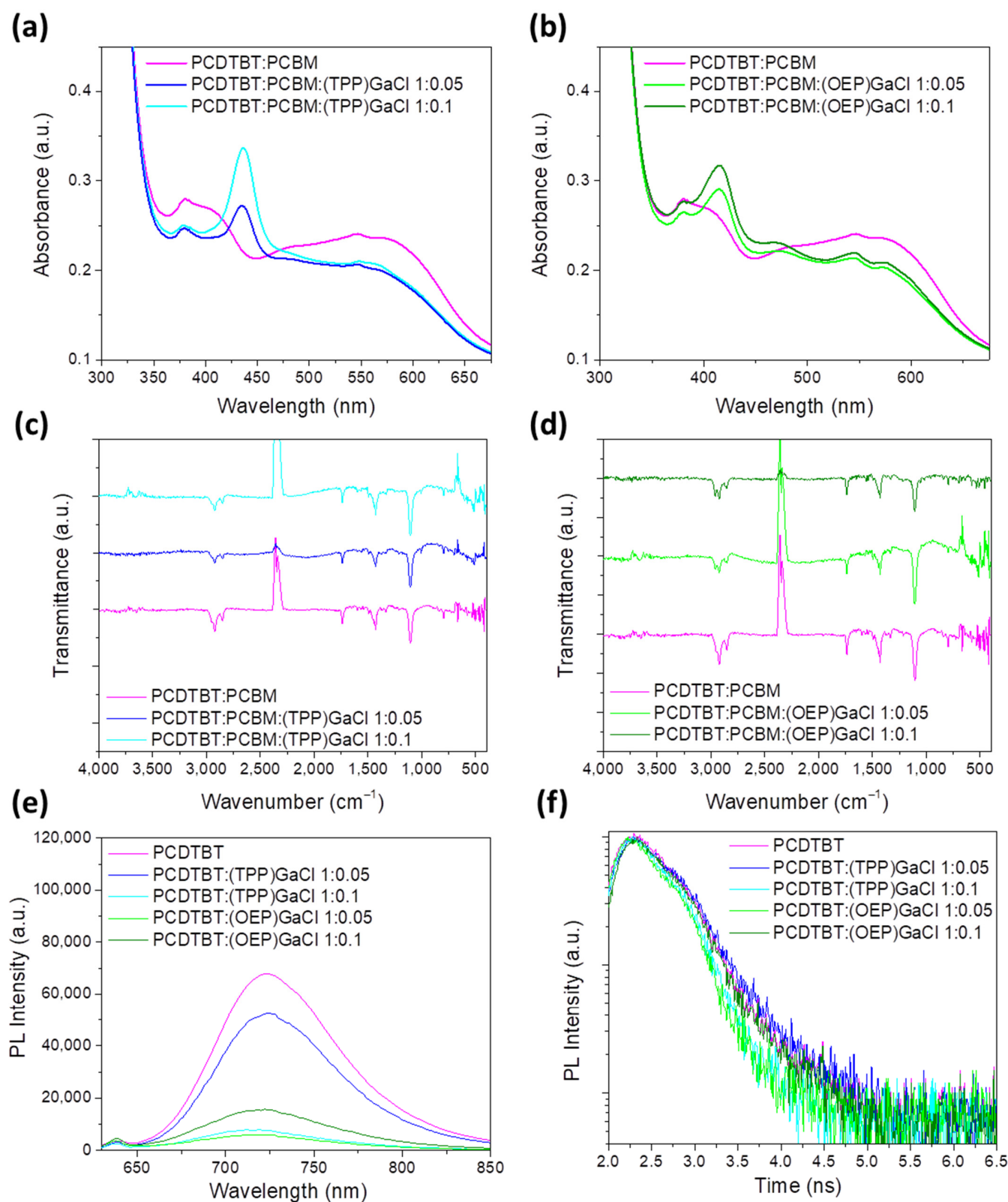


**Figure 3.** UV-Vis absorption spectra of binary and ternary PCDTBT:PCBM films with porphyrin additives: (a) (TPP)GaCl and (b) (OEP)GaCl in various ratios. FTIR spectra of binary and ternary PCDTBT:PCBM films with porphyrin additives: (c) (TPP)GaCl and (d) (OEP)GaCl in various ratios. (e) Steady-state PL spectra of PCDTBT without or with (TPP)GaCl and (OEP)GaCl in various ratios and (f) transient PL dynamics of the same samples.



Figure 3e shows the PL spectra of the PCDTBT and PCDTBT:(TPP)GaCl films demonstrating a significant decrease in emitted light intensity as the porphyrin concentration increases. Adding (TPP)GaCl in a ratio of 1:0.05 vv% reduces the fluorescence intensity of the PCDTBT film by 30%, and with a ratio of 1:0.1 vv% the fluorescence is almost completely suppressed by 88%. The most pronounced quenching occurs with (OEP)GaCl, likely due to the aggregation of its molecules, which serves as an additional factor in reducing the fluorescence. Photoluminescence quenching indicates efficient energy transfer from the polymer PCDTBT to the porphyrin compound. However, despite the quenching effect, a shift towards shorter wavelengths (blue shift) is observed in the PCDTBT emission spectrum after incorporating the porphyrins. This shift could be attributed to the mitigation of charge-carrier-trapping states within the porphyrin, resulting in a modified emission for PCDTBT. PL shift also indicates that the trap-assisted recombination mechanism is dominated in the ternary photoactive layers. Furthermore, time-resolved PL (TRPL) measurements, presented in Figure 3f for the PCDTBT:(TPP)GaCl and PCDTBT:(OEP)GaCl, show a shorter exciton life time, suggesting the faster exciton dissociation, especially in the case of the PCDTBT:(TPP)GaCl 1:0.1 and PCDTBT:(OEP)GaCl 1:0.05 samples. In the case of the P3HT blended with the two GaCl-porphyrins (Figure S1f), a short exciton lifetime, facilitating exciton dissociation, exhibits only the P3HT:(TPP)GaCl film.

In order to study the surface nanomorphology of the ternary films, atomic force microscopy (AFM) measurements were performed. Figures 4 and S2 depict the  $5 \times 5 \mu\text{m}^2$  surface topographic AFM image of pristine PCDTBT:PCBM and P3HT:PCBM films, respectively, as well as the films of these photoactive blends modified with (TPP)GaCl and (OEP)GaCl in ratios of 1:0.05 and 1:0.1. AFM analysis of the PCDTBT:PCBM film (Figure 4a) revealed that the introduction of (TPP)GaCl in both concentrations (1:0.05 and 1:0.1) slightly changed the surface roughness of the samples exhibiting root mean square (RMS) roughness of 1.63 nm and 1.00 nm for the PCDTBT:PCBM:(TPP)GaCl 1:0.05 (Figure 4b) and PCDTBT:PCBM:(TPP)GaCl 1:0.1 (Figure 4c), respectively, compared with the RMS = 0.99 of the binary film. However, small grains of a few nanometers, which may be assigned to the porphyrin compound, are observed on the surface of the ternary films. On the other hand, the nanomorphology of the ternary films based on the (OEP)GaCl porphyrin is significantly changed. The surface of the PCDTBT:PCBM:(OEP)GaCl (Figure 4d,e) consists of large domains, with size  $\sim 500$  nm for the PCDTBT:PCBM:(OEP)GaCl 1:0.1 and RMS = 14.94 nm. A similar trend in the surface nanomorphology of the porphyrin-modified P3HT:PCBM film is also observed (Figure S2a–e). The pristine P3HT:PCBM film exhibited a smooth surface with RMS = 0.99 nm, while the incorporation of (TPP)GaCl resulted in a slightly rough surface with small grains. However, the addition of (OEP)GaCl in the binary P3HT:PCBM resulted in phase separation of the materials consisting of the ternary films along with large domains and rougher surfaces, with RMS of 8.62 nm and 20.09 nm for the P3HT:PCBM:(OEP)GaCl 1:0.05 and P3HT:PCBM:(OEP)GaCl 1:0.1 films, respectively. On the other hand, the incorporation of gallium-porphyrins in the binary P3HT:PCBM blend significantly affected the crystallinity of the ternary films. Figure S2f shows the XRD patterns of binary and P3HT:PCBM-based ternary films. It is observed that P3HT:PCBM:(TPP)GaCl 1:0.05 exhibit improved crystallinity with a larger crystalline size of 7.9 nm (estimated with the Scherrer equation) compared with 6.1 nm for the binary blend. However, a higher concentration of (TPP)GaCl (1:0.1) in the binary film suppresses the crystallization of the ternary film. Crystallinity suppression of the P3HT:PCBM-based ternary films was also observed upon incorporation of the (OEP)GaCl in the binary blend, which may affect charge transport in the ternary film. On the other hand, due to the amorphous nature of the PCDTBT polymer, it was not possible to extract similar results from the corresponding X-ray diffraction diagrams (Figure 4f), where no changes in the crystallinity of the PCDTBT:PCBM are observed when (TPP)GaCl or (OEP)GaCl introduced in the binary blend.

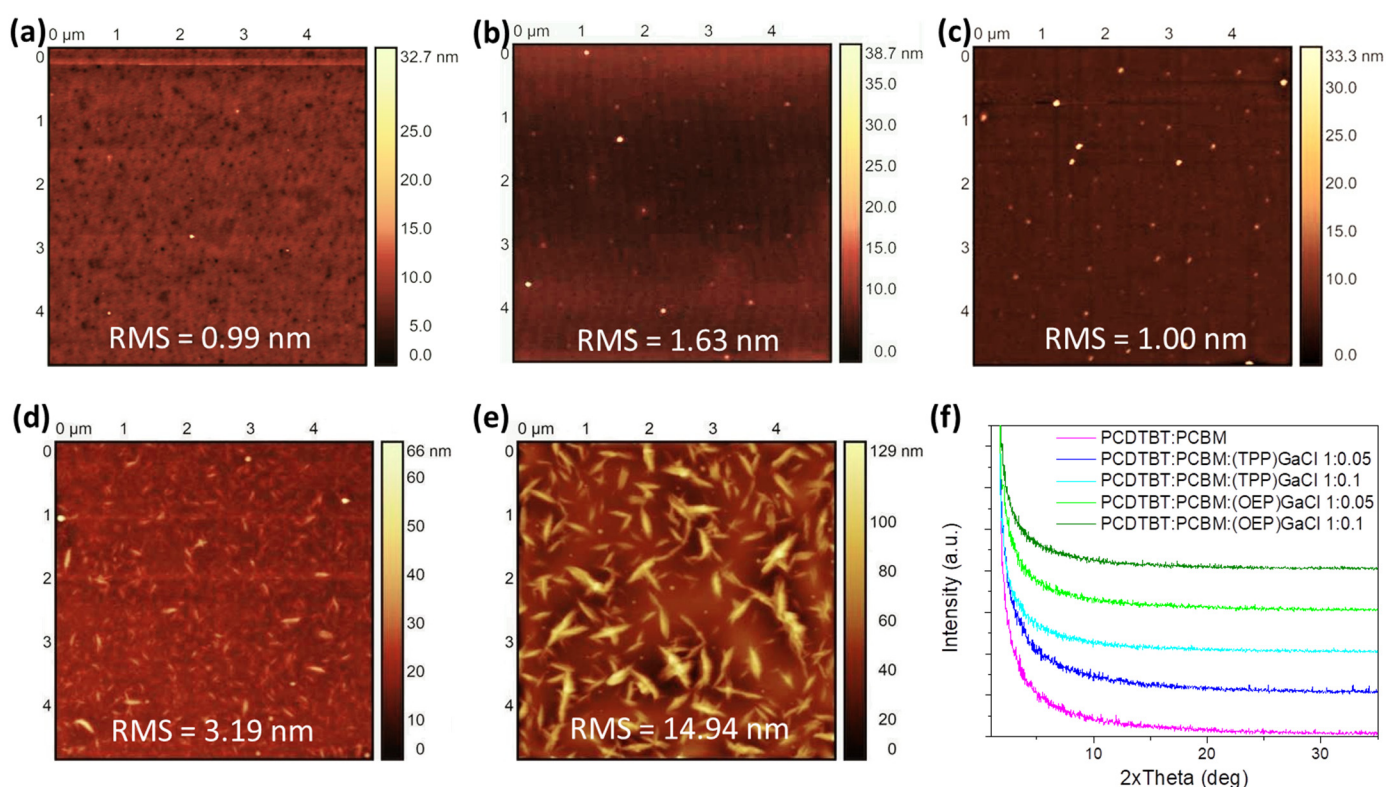


**Figure 4.**  $5 \times 5 \mu\text{m}^2$  AFM height images of (a) binary PCDTBT:PCBM, (b) PCDTBT:PCBM:(TPP)GaCl 1:0.05 (c) PCDTBT:PCBM:(TPP)GaCl 1:0.1, (d) PCDTBT:PCBM:(OEP)GaCl 1:0.05 and (e) PCDTBT:PCBM:(OEP)GaCl 1:0.1 ternary blended films. (f) XRD patterns of the same samples.

In order to investigate the compatibility of the two porphyrins with the donor and acceptor materials, the surface energies of the neat (TPP)GaCl, (OEP)GaCl, PCDTBT, P3HT and PCBM films were measured. The surface energy of material X ( $\gamma_X$ ) was estimated using contact angle measurements. The contact angle of deionized and diiodomethane droplets on the porphyrins PCDTB, P3HT and PCBM's films are shown in Figure S3, and the surface energy of each material is summarized in Table S1. The surface energy of (TPP)GaCl ( $\sim 41 \text{ mN m}^{-1}$ ) is closer to that of the donor and acceptor materials ( $\sim 40.2$ ,  $45.7$ , and  $49.5 \text{ mN m}^{-1}$ , for the P3HT, PCDTBT and PCBM, respectively) than that of the (OEP)GaCl suggesting that the porphyrin (TPP)GaCl has good miscibility with the BHJ materials [77,78]. On the other hand, (OEP)GaCl film exhibits a high surface energy ( $68.1 \text{ mN m}^{-1}$ ) leading to phase separation and the formation of large aggregates. The location of the porphyrins in the binary blended films P3HT:porphyrin, PCDTBT:porphyrin and PCBM:porphyrin were also investigated. Figures S4–S6 show the contact angle measurements of the binary films P3HT:porphyrin, PCDTBT:porphyrin and PCBM:porphyrin, and Figure S7a,b shows the surface energy of the binary films versus the concentrations of (TPP)GaCl and (OEP)GaCl, respectively. It is observed that the surface energy of binary films based on a (TPP)GaCl porphyrin compound is similar to those of neat PCDTBT, P3HT and PCBM films. Therefore, we next estimated the wetting coefficient ( $\omega$ ) for the ternary films to predict the location of the porphyrins in them using Young's equation [79]. Figures S8 and S9 present the contact angle measurements of the P3HT:PCBM and PCDTBT:PCBM based ternary films with (TPP)GaCl and (OEP)GaCl as the third component. As shown in Table S2, the  $\omega$  in the all ternary blends (PCDTBT:PCBM:(TPP)GaCl, PCDTBT:PCBM:(OEP)GaCl, P3HT:PCBM:(TPP)GaCl and P3HT:PCBM:(OEP)GaCl) is between  $-1$  and  $1$  ( $-1 < \omega < 1$ ), demonstrating that the porphyrin compound is located at the donor/acceptor interface [80], which could improve charge transfer in the ternary OSCs.

Another goal, apart from the optoelectronic, morphological and structural investigation of GaCl porphyrins-based ternary films, was the stability study of the prepared films under constant illumination conditions. Therefore, binary and ternary films were exposed to sunlight illumination in ambient conditions, and UV-Vis and FTIR spectroscopy, along with XRD measurements, were performed. To assess the degree to which porphyrins contribute to the long-term stability of each photoactive film under ambient conditions, it was necessary to conduct an investigation into the samples when traces of oxygen or humidity were present. Figure 5 shows the UV-Vis absorption spectra of pristine PCDTBT:PCBM and porphyrin-modified blend films, where no differences before and after their exposure to 8 h of sunlight illumination are noticed, indicating no degradation of the binary and ternary films. On the other hand, in the case of P3HT:PCBM:GaCl (Figure S10) a blue shift of  $\sim 10$  nm of the three main peaks of P3HT after exposure to sunlight illumination for 8 h can be seen. Note that the peak corresponding to the Soret band of the GaCl porphyrins remains unaffected.

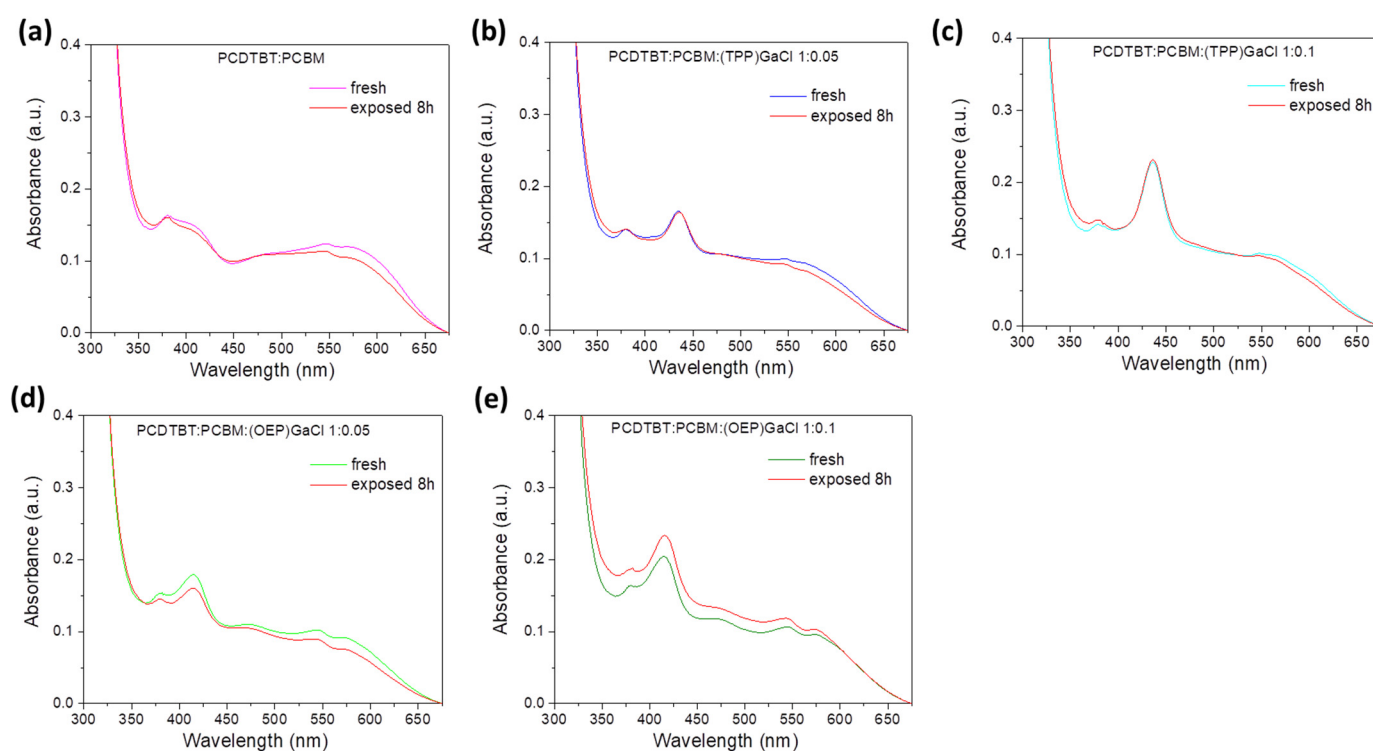


**Figure 5.** UV-Vis absorption spectra of fresh and exposed to sunlight illumination for 8 h of (a) binary PCDTBT:PCBM and ternary (b) PCDTBT:PCBM:(TPP)GaCl 1:0.05, (c) PCDTBT:PCBM:(TPP)GaCl 1:0.1, (d) PCDTBT:PCBM:(OEP)GaCl 1:0.05, and (e) PCDTBT:PCBM:(OEP)GaCl 1:0.1 films.

Figures S11 and S12 show the FTIR transmittance spectra of fresh and exposed to sunlight illumination for 8 h of the P3HT:PCBM:GaCl and PCDTBT:PCBM:GaCl films, respectively. According to Figure S11a, the peak at  $820\text{ cm}^{-1}$  for the P3HT:PCBM photoactive film is slightly shifted to higher energies when the film is exposed to sunlight illumination (8 h), suggesting a suppression of charge transfer from sulfur atoms of P3HT to PCBM. Moreover, the P3HT:PCBM:(TPP)GaCl and P3HT:PCBM:(OEP)GaCl films remain stable upon sunlight illumination as no significant changes in the FTIR spectra are observed (Figure S11b–e). In the case of PCDTBT:PCBM-based binary and ternary films, FTIR analysis of all spectra (Figure S12a–e) reveals that there are no noticeable changes even after 8 h of light exposure.

More interestingly, the P3HT:PCBM:(TPP)GaCl film exhibited better structural stability upon porphyrin compared with the P3HT:PCBM film. Figure 6a,b shows the XRD patterns of the fresh and exposed P3HT:PCBM and P3HT:PCBM:(TPP)GaCl films, respectively. In the

case of the binary film, the diffraction peak at  $2\theta = 5.16^\circ$  attributed to the (100) plane of P3HT is shifted to lower angle values ( $2\theta = 4.7^\circ$ ) resulting in increased d-spacing (from 1.71 nm to 1.88 nm) and a reduced crystalline size of  $\sim 2.4$  nm, thus degradation of the exposed P3HT:PCBM film to sunlight illumination. On the other hand, P3HT:PCBM:(TPP)GaCl 1:0.05 is more resistant to sunlight, since a small change in its crystallinity is observed. In particular, the d-spacing is slightly increased from 1.71 nm to 1.73 nm (estimated by Bragg law, where  $2\theta = 5.1^\circ$ ), while the crystalline size is reduced to  $\sim 5.5$  nm (crystalline size of fresh film was 7.9 nm), indicating improved photostability.

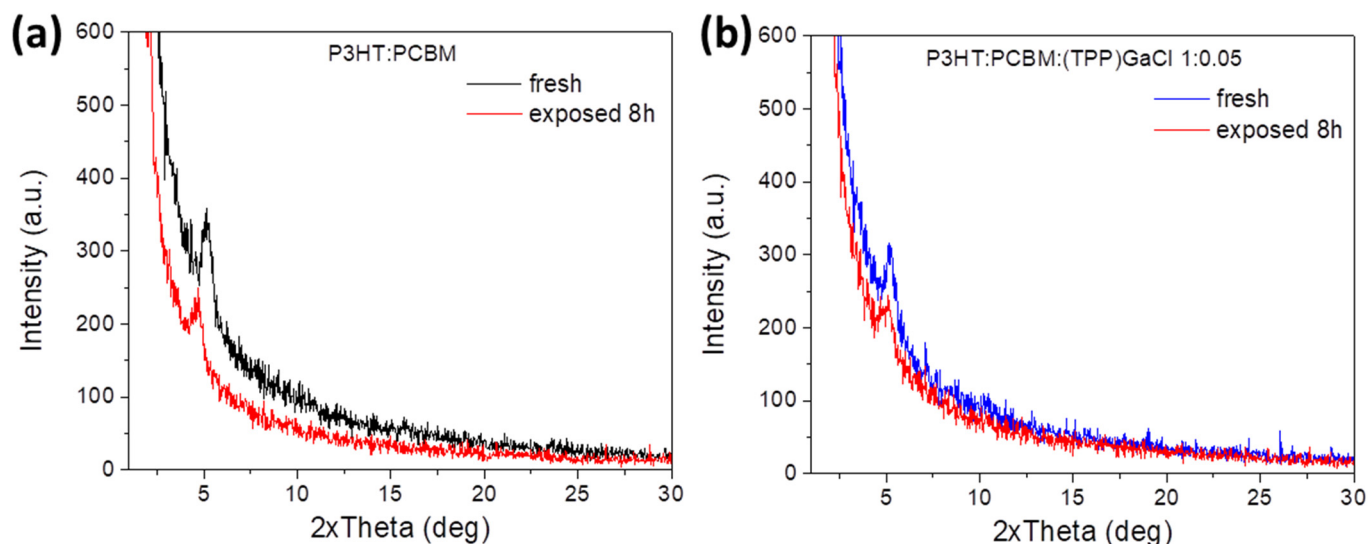


**Figure 6.** XRD patterns of fresh and exposed to sunlight illumination for 8 h of (a) binary P3HT:PCBM and ternary (b) P3HT:PCBM:(TPP)GaCl 1:0.05 films.

### 2.3. Fabrication of Ternary-Based Organic Solar Cells

According to these results, organic solar cells (OSCs) with ternary photoactive layers based on (TPP)GaCl porphyrin of low concentration (1:0.05) were prepared. The device structure shown in Figure 7a along with the chemical structure of the polymer donors and fullerene acceptor constituting the active layer was ITO/PEDOT:PSS/P3HT:PCBM:(TPP)GaCl 1:0.05/Al or ITO/PEDOT:PSS/PCDTBT:PCBM:(TPP)GaCl 1:0.05/Al. Note that OSCs with binary photoactive layers (without the addition of the (TPP)GaCl porphyrin) were also fabricated for comparison reasons. Figure 7b,c depict the current density–voltage characteristic curves of binary and ternary OSCs based on the PCDTBT:PCBM and P3HT:PCBM blends, respectively. Enhanced device performance of about  $\sim 17\%$  is observed for the ternary devices with the (TPP)GaCl porphyrin as the third component of the active layer, compared to the binary OSCs. In particular, the device with the ternary PCDTBT:PCBM:(TPP)GaCl 1:0.05 active layer exhibited higher short-circuit current density ( $J_{SC}$ ) and fill factor (FF) values of  $11.14 \text{ mA cm}^{-2}$  and 0.53, respectively, and thus lead to a higher power conversion efficiency (PCE) value of 4.61%, compared with the corresponding binary (PCDTBT:PCBM) OSC with  $J_{SC} = 10.66 \text{ mA cm}^{-2}$ ,  $FF = 0.48$ , and  $PCE = 3.94\%$  (Table 2). It is noted that this PCE enhancement is independent from the ternary film thickness since the insertion of porphyrin of low concentration in the binary blend did not change it. In the same context, improved  $J_{SC}$  of  $12.90 \text{ mA cm}^{-2}$ , FF of 0.54, and PCE of 4.25% are observed for the P3HT:PCBM:(TPP)GaCl 1:0.05 device, while the binary OSC without the porphyrin compound exhibited lower values ( $J_{SC} = 12.09 \text{ mA cm}^{-2}$ ,  $FF = 0.50$ , and  $PCE = 3.63\%$ ). These results were highly reproducible as shown in Figures S13 and S14, where the statistical errors and the standard box plots of the  $J_{SC}$ ,  $V_{OC}$ , FF and PCE values resulting from the measurements in a batch of 12 identical devices for each kind are presented. The  $J_{SC}$  and FF enhancement suggests reduced recombination losses when the

(TPP)GaCl porphyrin with low concentration is inserted in the active layer, which is also supported by the PL measurements (Figures 3e,f and S1e,f), as well as the higher shunt resistance ( $R_{SH}$ ) and the lower series resistance ( $R_S$ ) of the ternary OSCs compared with the binary devices, also summarized in Table 2. PL quenching indicates charge transfer between the polymer-donor (PCDTBT or P3HT) and the porphyrin (TPP)GaCl, which is also supported by the increased FF [81]. In addition, it is known that  $R_{SH}$  is related to charge recombination; therefore, higher  $R_{SH}$  values in the ternary OSCs reflects the suppression of trap-assisted recombination resulting in the enhancement of FF, and thus in the ternary OSCs PCE value. Note that an insignificant improvement in the  $V_{OC}$  of the ternary devices is also observed and assigned to the slight influence of the (TPP)GaCl 1:0.05 on the nanomorphology and crystallinity of the ternary films, as revealed in the AFM and XRD measurements. On the other hand, when the concentration of the (TPP)GaCl increased (1:0.01), a lower performance of the ternary OSCs was obtained, as shown in Figure S15. Poor electrical parameters were also observed for the ternary devices based on the (OEP)GaCl porphyrin (Figure S15), which can be attributed to the rougher surface morphology and the suppressed crystallinity of the ternary active layers (Figures 4 and S2). The formation of large aggregates in the ternary films were observed when porphyrin compounds with high concentration were inserted in the binary photoactive films, which hindered exciton generation and charge separation, thus leading to lower PCE values.

The reduced recombination of charge carriers in the ternary photoactive films compared with the binary layers was also confirmed by measuring the J-V characteristic curves of the OSCs under dark condition, which are shown in Figure S16. It is observed that the dark current density ( $J_{DARK}$ ) of the ternary OSCs at the reverse bias is reduced in respect to the binary device suggesting the suppression of the charge carriers in the ternary layer since the  $J_{DARK}$  is an indication of charge carrier recombination. Furthermore, the ternary devices exhibit higher  $J_{DARK}$  at forward bias compared with the binary OSCs leading to decreased  $R_S$ . Lower  $R_S$  values favor charge extraction in the ternary OSCs. Additionally, the ideality factor of the ternary devices is improved (especially in the case of PCDTBT:PCBM-based OSCs), suggesting reduced charge carrier recombination.

To further support that the (TPP)GaCl porphyrin acts as an electron cascade material when inserted in the binary PCDTBT:PCBM and/or P3HT:PCBM blends leading to improved charge transport, external quantum efficiency (EQE) measurements were performed. The EQE spectra of the ternary OSCs based on the PCDTBT:PCBM:(TPP)GaCl 1:0.05 and P3HT:PCBM:(TPP)GaCl 1:0.05 active layer along with the EQE spectra of the corresponding binary devices are shown in Figure 7d,e, respectively. It is observed that although the (TPP)GaCl porphyrin contributes to the absorption of the ternary films (Figures 3a and S1a), the light harvesting of the ternary OSCs remained unaffected by the insertion of the (TPP)GaCl in the BHJ blend (PCDTBT or P3HT). The shape of EQE spectra of the binary and ternary devices exhibited no changes; however, the ternary OSCs showed improved EQE compared with the binary devices, which could be attributed to the formation of an efficient cascade system in the ternary layers. Moreover, the  $J_{SC}$  of all OSCs estimated by the EQE measurements are  $10.42 \text{ mA cm}^{-2}$  and  $11.05 \text{ mA cm}^{-2}$  for the PCDTBT:PCBM and PCDTBT:PCBM:(TPP)GaCl devices, respectively, while for the P3HT:PCBM based OSCs the  $J_{SC}$  for the binary and ternary devices was  $11.61 \text{ mA cm}^{-2}$  and  $12.25 \text{ mA cm}^{-2}$ , respectively. This small difference (less than 5%) between the measured and estimated  $J_{SC}$  suggest the very good accuracy of the fabricated OSCs electrical characterization measurements.

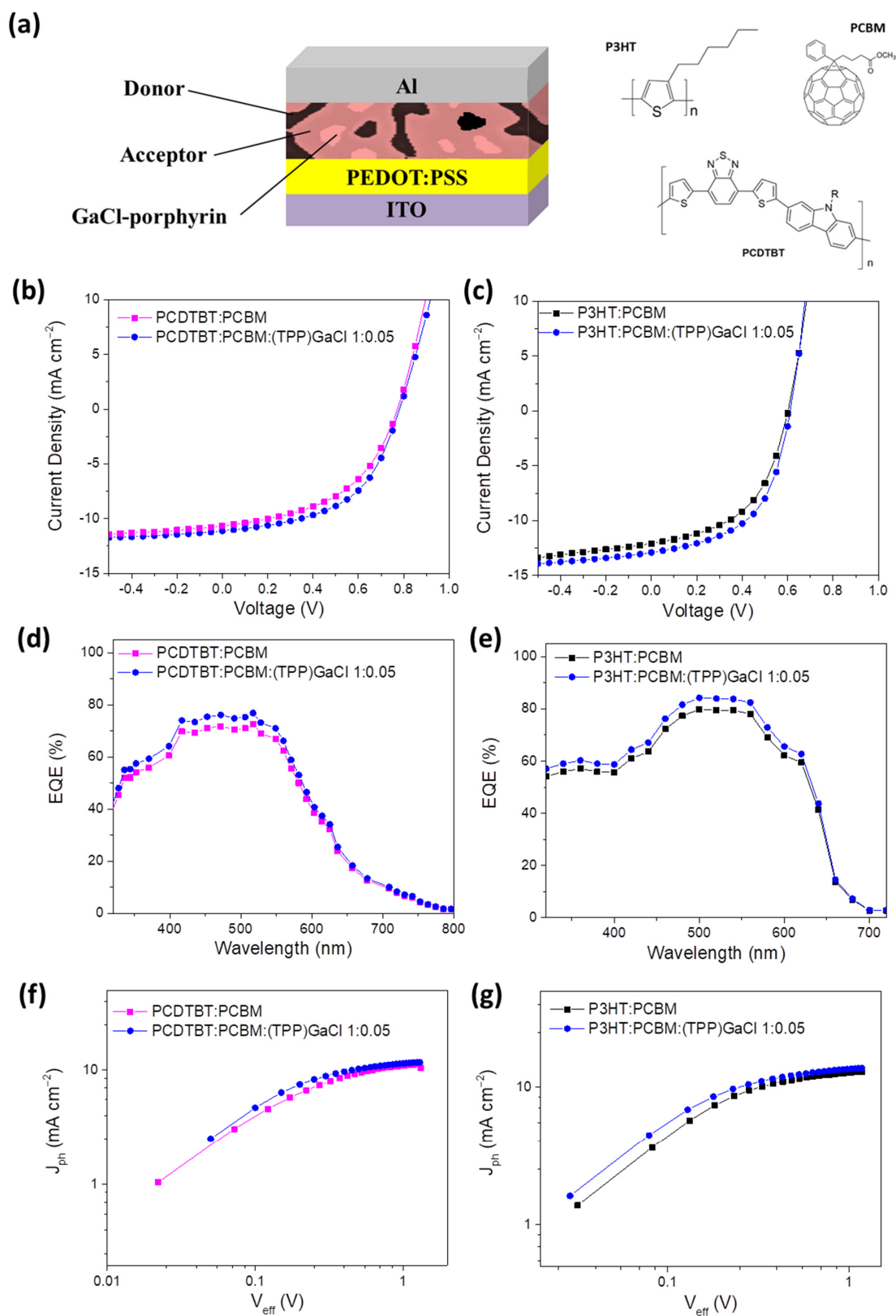


**Figure 7.** (a) Device structure and chemical structure of the donor and acceptor organic materials used in the photoactive layer of the ternary OSCs. J-V characteristic curves under 1.5 AM illumination of ternary OSCs based on (b) PCDTBT:PCBM:(TPP)GaCl 1:0.05 and (c) P3HT:PCBM:(TPP)GaCl 1:0.05 layers. J-V curves of binary devices are also depicted. (d,e) EQE spectra of the same devices. (f,g) Variation of photocurrent density ( $J_{ph}$ ) with effective voltage ( $V_{eff}$ ) of the same devices.

**Table 2.** Electrical parameters of the fabricated OSCs estimated by the J-V characteristic curves shown in Figure 7b,c (mean values and standard deviations were extracted from a batch of 12 independent devices).

Active Layer	$J_{SC}$ ( $\text{mA cm}^{-2}$ )	$V_{OC}$ (V)	FF	$PCE_{aver.}$ (%)	$R_S$ ( $\Omega \text{ cm}^2$ )	$R_{SH}$ ( $\Omega \text{ cm}^2$ )
PCDTBT:PCBM	−10.66	0.77	0.48	3.94	11.5	401
PCDTBT:PCBM:(TTP)GaCl 1:0.05	−11.14	0.78	0.53	4.61	8.2	489
P3HT:PCBM	−12.09	0.60	0.50	3.63	5.3	289
P3HT:PCBM:(TTP)GaCl 1:0.05	−12.90	0.61	0.54	4.25	3.7	318

In order to investigate the influence of (TPP)GaCl porphyrin on the charge generation efficiency, photocurrent density ( $J_{PH}$ ) versus effective voltage ( $V_{EFF}$ ) were plotted.  $J_{ph}$  is estimated from  $J_{PH} = J_{ILL} - J_{DARK}$ , where  $J_{ILL}$  and  $J_{DARK}$  are the current density values under illumination and in dark condition, respectively.  $V_{EFF}$  is defined as  $V_{EFF} = V_0 - V$ , where  $V_0$  is the voltage at which the  $J_{PH}$  is zero and  $V$  is the applied voltage. The estimated results of the binary and ternary OSCs based on the PCDTBT:PCBM and P3HT:PCBM blends are shown in Figure 7f,g, respectively. It is observed that the ternary OSCs with the (TPP)GaCl porphyrin exhibit higher  $J_{PH}$  values at low  $V_{EFF}$  compared with the corresponding binary devices, suggesting improved exciton dissociation into free carriers. In addition, both ternary OSCs show higher charge dissociation probabilities ( $P(E,T)-V_{EFF}$  presented in Figure S17) and charge collection efficiency (estimated from  $J_{PH}/J_{PH,SAT}$ , where  $J_{PH,SAT}$  is the saturated  $J_{PH}$ ) at short-circuit and at the maximum power point, respectively, than the binary devices. Moreover, at high  $V_{EFF}$  values ( $V_{EFF} > 1$ ), the  $J_{PH,SAT}$  of the ternary OSCs is higher than those of the binary ones, resulting in an enhanced exciton generation rate ( $G_{MAX}$ , estimated by the  $G_{MAX} = J_{PH,SAT}/qL$ , where  $q$  is the elementary charge and  $L$  is the thickness of the photoactive layer) when (TPP)GaCl porphyrin is inserted in the binary blends. The higher exciton dissociation and charge extraction probabilities are consistent with the increase in FF in the ternary OSCs.

Other than the device efficiency, the photostability of the (TPP)GaCl-based ternary OSCs was also investigated by exposing the fabricated binary and ternary OSCs to sunlight illumination for 8 h without any encapsulation. Figure 8 shows the variation of normalized PCE values over a period of 8 h illumination for the binary and ternary OSCs. It is observed that the PCDTBT:PCBM:(TPP)GaCl 1:0.05-based OSC retained over 85% of its initial PCE value, while the efficiency of the binary device decreased to ~71% after exposure to sunlight for 8 h (Figure 8a). Similar results were also obtained for the ternary P3HT:PCBM-based OSC, where the P3HT:PCBM:(TPP)GaCl 1:0.05 device exhibited enhanced photostability (retain the ~86% of its initial PCE value) compared with the exposed binary P3HT:PCBM OSC with its PCE decreasing to ~73% of its initial efficiency value (Figure 8b). This improved photostability can be attributed to the suppressed degradation, better nanomorphology and crystallinity of the ternary films after being exposed to sunlight illumination for 8 h.

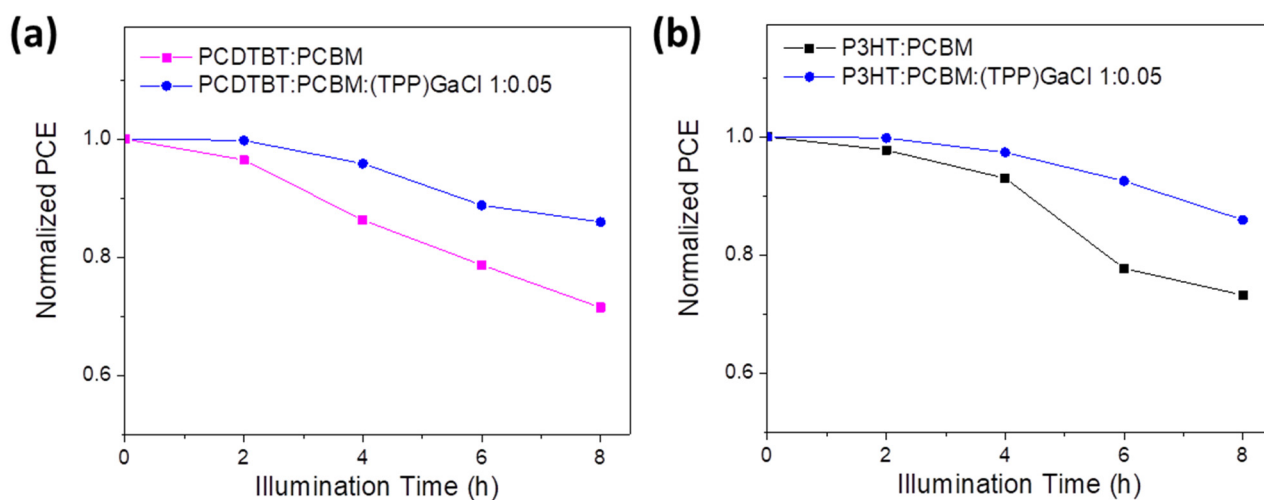


**Figure 8.** Stability study of binary and ternary OSCs. Normalized PCE values versus illumination time of OSCs based on (a) PCDTBT:PCBM:(TPP)GaCl 1:0.05 and (b) P3HT:PCBM:(TPP)GaCl 1:0.05 layers, compared with the corresponding binary devices.

### 3. Conclusions

In conclusion, ternary air-processed photoactive layers consisting of a polymer donor (PCDTBT or P3HT) and a fullerene acceptor (PCBM) have been prepared using two GaCl-based porphyrins as the third component. Electrochemical measurements revealed a good energy level alignment between both gallium porphyrins, polymer donors (PCDTBT or P3HT) and the PCBM acceptor forming an efficient cascade system that could facilitate electron transfer between donor and acceptor. Therefore, ternary OSCs were fabricated. It was shown that the devices with the (TPP)GaCl 1:0.05 (i.e., PCDTBT:PCBM:(TPP)GaCl 1:0.05 or P3HT:PCBM:(TPP)GaCl 1:0.05) exhibited increased  $J_{SC}$  and FF, and thus higher PCE compared to the corresponding binary OSCs, assigned to the reduced trap-assisted recombination and improved exciton dissociation. On the other hand, the devices with higher (TPP)GaCl concentration (1:0.1), as well as the OSCs based on (OEP)GaCl, exhibited low performance due to the significant alteration of the nanomorphology of the ternary films with very rough surfaces and the suppressed crystalline formation. The devices with the (TPP)GaCl 1:0.05-ternary layer also exhibited enhanced photostability when the OSC was exposed to sunlight illumination, maintaining the ~85% of the initial PCE value after 8 h, which is attributed to the better crystallinity and suppressed photodegradation of the ternary photoactive film. The proposed ternary approach presents a simple low-cost solution-processed strategy under ambient conditions to improve OSC efficiency which could also be compatible with recyclable substrates for sustainable, scalable and environmentally friendly energy production.

### 4. Experimental Section

**Film preparation.** Binary P3HT:PCBM (1:0.8 wt% ratio) and PCDTBT:PCBM (1:4 wt% ratio) films were prepared by spin-coating the binary blended solutions from 10 mg mL<sup>-1</sup> of chloroform under air conditions (40% humidity at 25 °C). For the ternary films, 5 mg of each porphyrin molecule were dissolved in 1 mL of chloroform. Then, binary:porphyrin 1:0.05 vv% ratio and 1:0.1 vv% ratio solutions were prepared forming the P3HT:PCBM:(TPP)GaCl, P3HT:PCBM:(OEP)GaCl, PCDTBT:PCBM:(TPP)GaCl and PCDTBT:PCBM:(OEP)GaCl films through spin-coating. In particular, PCDTBT:PCBM-based binary and ternary films were formed through spin-coating at 1000 rpm for 2 min followed by thermal annealing at 60 °C for 1 min. In the case of P3HT:PCBM and P3HT:PCBM:GaCl porphyrin, spin-coating was performed at 600 rpm for 40 s, and then the samples were placed on a hot plate at 135 °C for 10 min. The thickness of the P3HT:PCBM



and PCDBTB:PCBM-based films was  $100 \pm 8$  nm and  $150 \pm 5$  nm, respectively. Note that all films were prepared under ambient conditions (40% humidity at 25 °C).

**Thin film characterization methods.** The thickness of the binary and ternary films was measured with a profilometer. Fourier-transform infrared (FTIR) spectroscopy was performed using a Bruker Tensor 27 spectrometer equipped with a DTGS detector. Absorption spectra of the porphyrin, binary and ternary films were taken with a Perkin Elmer Lambda 40 UV-Vis spectrometer. Cyclic voltammetry of the two porphyrin molecules deposited on glass/ITO substrates were obtained with a VersaSTAT 4 potentiometer operating at a scan rate of  $0.1 \text{ V s}^{-1}$ ; the solvent was acetonitrile containing 0.1M  $\text{LiClO}_4$  as the electrolyte, while Ag/AgCl was the reference electrode. Steady-state photoluminescence (PL) spectra were recorded with a commercial platform (ARKEO—Cicci Research); the substrate was illuminated with a diode-pumped solid-state Nd:YVO<sub>4</sub> + KTP laser (peak wavelength  $532 \text{ nm} \pm 1 \text{ nm}$ , with optical power of 1 mW on a circular spot of 2 mm in diameter:  $31 \text{ mW cm}^{-2}$ ) at an inclination of 45°. The fluorescence on the opposite side of the substrate was focused on a bundle of fibers (10 mm in diameter) with an aspheric lens close to the substrate to maximize the PL. The bundle sends the signal to a CCD-based spectrometer. Integration time and the number of averaging was maintained the same to better compare the results. Time-resolved PL (TRPL) spectra were measured with an FS5 spectrofluorometer from Edinburgh Instruments using a 478.4 nm laser as an excitation source. The surface morphology of the binary P3HT:PCBM and PCDTBT:PCBM and ternary P3HT:PCBM:porphyrin and PCDTBT:PCBM:porphyrin films was investigated with atomic force microscopy (AFM) using an NT-MDT AFM system in tapping operation mode. X-ray diffractograms (XRD) were recorded using a Siemens D500 diffractometer with  $\text{Cu K}\alpha$  radiation.

**OSCs fabrication and characterization.** Indium tin oxide (ITO, coated on glass substrates, were cleaned by sonication in a deionized water, acetone and isopropyl bath for 10 min each. Then, they were subjected to UV-ozone for 20 min. Next, a PEDOT:PSS (poly(3,4-ethylenedioxythiophene)–poly(styrenesulfonate)) solution filtered with a  $0.45 \mu\text{m}$  PVDF (polyvinylidene fluoride) filter was spin-coated on the ITO at 4000 rpm for 45 s, and the prepared films were placed on a hotplate at 150 °C for 30 min. Air-processed PCDTBT:PCBM and P3HT:PCBM with and without the GaCl porphyrins were spin-coated on PEDOT:PSS to prepare the ternary and binary organic solar cells. The devices completed with the deposition of aluminum served as the cathode electrode. The current density–voltage (J–V) characteristic curves of the all, binary and ternary OSCs were measured with a Keithley 2400 source-meter in the dark and under illumination with intensity of  $100 \text{ mW cm}^{-2}$  using a Xe lamp as the illumination source equipped with a AM 1.5G filter in ambient conditions. To accurately define the active area of all devices, we used aperture masks during the measurements with their area equal to those of the Al contacts ( $12.56 \text{ mm}^2$ ).

**Supplementary Materials:** The following are available online at <https://www.mdpi.com/article/10.3390/nano13202800/s1>, Figure S1: UV-Vis absorption spectra of binary and ternary P3HT:PCBM films with porphyrin additives: (a) (TPP)GaCl and (b) (OEP)GaCl in various ratios. FTIR spectra of binary and ternary P3HT:PCBM films with porphyrin additives: (c) (TPP)GaCl and (d) (OEP)GaCl in various ratios. (e) Steady-state PL spectra of P3HT without or with (TPP)GaCl and (OEP)GaCl in various ratios and (f) Transient PL dynamics of the same samples; Figure S2:  $5 \times 5 \mu\text{m}^2$  AFM height images of (a) binary P3HT:PCBM, (b) P3HT:PCBM:(TPP)GaCl 1:0.05 (c) P3HT:PCBM:(TPP)GaCl 1:0.1, (d) P3HT:PCBM:(OEP)GaCl 1:0.05 and (e) P3HT:PCBM:(OEP)GaCl 1:0.1 ternary blended films. (f) XRD patterns of the same samples; Figure S3: Contact angle measurements of deionized water and diiodomethane droplets on P3HT, PCBM, PCDTBT, (TPP)GaCl, and (OEP)GaCl films deposited on glass substrates; Figure S4: Contact angle measurements of deionized water and diiodomethane droplets on binary P3HT:(TPP)GaCl and P3HT:(OEP)GaCl films deposited on glass substrates; Figure S5: Contact angle measurements of deionized water and diiodomethane droplets on binary PCDTBT:(TPP)GaCl and PCDTBT:(OEP)GaCl films deposited on glass substrates; Figure S6: Contact angle measurements of deionized water and diiodomethane droplets on binary PCBM:(TPP)GaCl and PCBM:(OEP)GaCl films deposited on glass substrates; Figure S7: Sur-

face energy of (a) P3HT:(TPP)GaCl, PCDTBT:(TPP)GaCl, and PCBM:(TPP)GaCl binary films, and (b) P3HT:(OEP)GaCl, PCDTBT:(OEP)GaCl, and PCBM:(OEP)GaCl binary films. The solid black line represents the surface of the neat porphyrin; Figure S8: Contact angle measurements of deionized water and diiodomethane droplets on binary P3HT:PCBM and ternary P3HT:PCBM:porphyrin-GaCl films deposited on glass substrates; Figure S9: Contact angle measurements of deionized water and diiodomethane droplets on binary PCDTBT:PCBM and ternary PCDTBT:PCBM:porphyrin-GaCl films deposited on glass substrates; Figure S10: UV-Vis absorption spectra of fresh and exposed to sunlight illumination for 8 h of (a) binary P3HT:PCBM and ternary (b) P3HT:PCBM:(TPP)GaCl 1:0.05, (c) P3HT:PCBM:(TPP)GaCl 1:0.1, (d) P3HT:PCBM:(OEP)GaCl 1:0.05, and (d) P3HT:PCBM:(OEP)GaCl 1:0.1 films; Figure S11: FTIR spectra of fresh and exposed to sunlight illumination for 8 h of (a) binary P3HT:PCBM and ternary (b) P3HT:PCBM:(TPP)GaCl 1:0.05, (c) P3HT:PCBM:(TPP)GaCl 1:0.1, (d) P3HT:PCBM:(OEP)GaCl 1:0.05, and (d) P3HT:PCBM:(OEP)GaCl 1:0.1 films; Figure S12: FTIR spectra of fresh and exposed to sunlight illumination for 8 h of (a) binary PCDTBT:PCBM and ternary (b) PCDTBT:PCBM:(TPP)GaCl 1:0.05, (c) PCDTBT:PCBM:(TPP)GaCl 1:0.1, (d) PCDTBT:PCBM:(OEP)GaCl 1:0.05, and (e) PCDTBT:PCBM:(OEP)GaCl 1:0.1 films; Figure S13: Statistical analysis of the performance parameters of PCDTBT:PCBM and PCDTBT:PCBM:(TPP)GaCl OSCs (12 devices for each type): (a) Jsc, (b) Voc, (c) FF and (d) PCE; Figure S14: Statistical analysis of the performance parameters of PCDTBT:PCBM and P3HT:PCBM:(TPP)GaCl OSCs (12 devices for each type): (a) Jsc, (b) Voc, (c) FF and (d) PCE; Figure S15: J-V characteristic curves under 1.5 AM illumination of ternary OSCs based on (a) PCDTBT:PCBM and (b) P3HT:PCBM with (TPP)GaCl 1:0.1, (OEP)GaCl 1:0.05 and (OEP)GaCl 1:0.1; Figure S16: Dark J-V characteristics curves of the binary and ternary OSCs based on (a) PCDTBT:PCBM and (b) P3HT:PCBM blends; Figure S17: Exciton dissociation probability ( $P(E,T)$ ) versus the effective voltage ( $VE_{eff}$ ) of binary and ternary OSCs based on (a) PCDTBT:PCBM and (b) P3HT:PCBM blends; Table S1: Contact angle and surface energy of various films; Table S2: Wetting coefficient of (TPP)GaCl and (OEP)GaCl added in P3HT:PCBM and PCDTBT:PCBM blends.

**Author Contributions:** Investigation, M.V. (Maria Verouti), E.P., K.-K.A. and Z.G.; Writing—Original Draft, A.S., E.P. and Z.G.; Methodology, L.C.P., I.K., V.K. and P.A.; Formal Analysis, A.C.; Data Curation, A.C.; Conceptualization, A.G.C.; Writing—Review and editing, A.S. and M.V. (Maria Vasilopoulou); Supervision, M.V. (Maria Vasilopoulou) and P.A.; Project Administration, M.V. (Maria Vasilopoulou); Visualization, A.S., M.V. (Maria Vasilopoulou) and A.G.C. All authors have read and agreed to the published version of the manuscript.

**Funding:** This research was funded by the research project “HELIOKERAMOS”-MIS 5066858, funded by the Operational Programme (EPAnEK) “Competitiveness, Entrepreneurship and Innovation” (NSRF 2014-2020), under the special action “Industrial Materials” and co-financed by Greece and the European Union (European Regional Development Fund).

**Data Availability Statement:** The data that support the findings of this study can become available by the corresponding authors upon reasonable request.

**Acknowledgments:** This work was supported by the research project “HELIOKERAMOS”-MIS 5066858, funded by the Operational Programme (EPAnEK) “Competitiveness, Entrepreneurship and Innovation” (NSRF 2014-2020), under the special action “Industrial Materials” and co-financed by Greece and the European Union (European Regional Development Fund). This research was also supported by Grant 81365 from the Research Committee of the University of Patras via “C. CARATHEODORI” program.

**Conflicts of Interest:** The authors declare no conflict of interest.

## References

1. Yan, C.; Barlow, S.; Wang, Z.; Yan, H.; Jen, A.K.Y.; Marder, S.R.; Zhan, X. Non-fullerene acceptors for organic solar cells. *Nat. Rev. Mater.* **2018**, *3*, 18003. [[CrossRef](#)]
2. Bergqvist, J.; Österberg, T.; Melianas, A.; Aguirre, L.E.; Tang, Z.; Cai, W.; Ma, Z.; Kemerink, M.; Gedefaw, D.; Andersson, M.R.; et al. Asymmetric photocurrent extraction in semitransparent laminated flexible organic solar cells. *NPJ Flex. Electron.* **2018**, *2*, 4. [[CrossRef](#)]
3. Wadsworth, A.; Moser, M.; Marks, A.; Little, M.S.; Gasparini, N.; Brabec, C.J.; Baran, D.; McCulloch, I. Critical review of the molecular design progress in non-fullerene electron acceptors towards commercially viable organic solar cells. *Chem. Soc. Rev.* **2019**, *48*, 1596. [[CrossRef](#)] [[PubMed](#)]

4. Duan, L.; Elumalai, N.K.; Zhang, Y.; Uddin, A. Progress in Stability of Organic Solar Cells. *Sol. Energy Mater. Sol. Cells* **2019**, *193*, 22. [[CrossRef](#)]
5. Duan, L.; Yi, H.; Wang, Z.; Zhang, Y.; Haque, F.; Sang, B.; Deng, R.; Uddin, A. Semitransparent organic solar cells based on PffBT4T-2OD with a thick active layer and near neutral colour perception for window applications. *Sustain. Energy Fuels* **2019**, *3*, 2456. [[CrossRef](#)]
6. Sadasivuni, K.K.; Deshmukh, K.; Ahipa, T.N.; Muzaffar, A.; Ahamed, M.B.; Pasha, S.K.K.; Al-Maadeed, M.A.-A. Flexible, biodegradable and recyclable solar cells: A review. *J. Mater. Sci. Mater. Electron.* **2019**, *30*, 951. [[CrossRef](#)]
7. Wang, D.; Liu, J.; Li, Y.; Zhou, G.; Zhan, L.; Zhu, H.; Lu, X.; Chen, H.; Li, C.-Z. High-performance and eco-friendly semitransparent organic solar cells for greenhouse applications. *Joule* **2021**, *5*, 945. [[CrossRef](#)]
8. Li, Y.; Lin, J.D.; Che, X.; Qu, Y.; Liu, F.; Liao, L.-S.; Forrest, S.R. High efficiency near-infrared and semitransparent non-fullerene acceptor organic photovoltaic cells. *J. Am. Chem. Soc.* **2017**, *139*, 17114. [[CrossRef](#)]
9. Ravishankar, E.; Booth, R.E.; Saravitz, C.; Sederoff, H.; Ade, H.W.; O'Connor, B.T. Achieving net zero energy greenhouses by integrating semitransparent organic solar cells. *Joule* **2020**, *4*, 490. [[CrossRef](#)]
10. Xie, L.; Song, W.; Ge, J.; Tang, B.; Zhang, X.; Wu, T.; Ge, Z. Recent progress of organic photovoltaics for indoor energy harvesting. *Nano Energy* **2021**, *82*, 105770. [[CrossRef](#)]
11. Su, Y.-J.; Huang, S.-C.; Chen, T.-W.; Chueh, L.-C.; Cui, Y.; Hong, L.; Yao, H.; Hou, J.; Chen, J.-T.; Hsu, C.-S. Elucidating End-Group Modifications of Carbazole-Based Nonfullerene Acceptors in Indoor Applications for Achieving a PCE of over 20%. *ACS Appl. Mater. Interfaces* **2021**, *13*, 26247. [[CrossRef](#)]
12. Cui, Y.; Hong, L.; Hou, J. Organic Photovoltaic Cells for Indoor Applications: Opportunities and Challenges. *ACS Appl. Mater. Interfaces* **2020**, *12*, 38815. [[CrossRef](#)]
13. Ryu, H.S.; Park, S.Y.; Lee, T.H.; Kim, J.Y.; Woo, H.Y. Recent progress in indoor organic photovoltaics. *Nanoscale* **2020**, *12*, 5792. [[CrossRef](#)]
14. Jung, S.; Oh, J.; Yang, U.J.; Lee, S.M.; Lee, J.; Jeong, M.; Cho, Y.; Kim, S.; Baik, J.M.; Yang, C. 3D Cu ball-based hybrid triboelectric nanogenerator with non-fullerene organic photovoltaic cells for self-powering indoor electronics. *Nano Energy* **2020**, *77*, 105271. [[CrossRef](#)]
15. Jia, Z.; Chen, Z.; Chen, X.; Yao, J.; Yan, B.; Sheng, R.; Zhu, H.; Yang, Y.M. 19.34 cm<sup>2</sup> large-area quaternary organic photovoltaic module with 12.36% certified efficiency. *Photonics Res.* **2021**, *9*, 324. [[CrossRef](#)]
16. Qin, F.; Sun, L.; Chen, H.; Liu, Y.; Lu, X.; Wang, W.; Liu, T.; Dong, X.; Jiang, P.; Jiang, Y.; et al. 54 cm<sup>2</sup> Large-Area Flexible Organic Solar Modules with Efficiency Above 13%. *Adv. Mater.* **2021**, *33*, 2103017. [[CrossRef](#)]
17. Dong, X.; Jiang, Y.; Sun, L.; Qin, F.; Zhou, X.; Lu, X.; Wang, W.; Zhou, Y. Large-Area Organic Solar Modules with Efficiency Over 14%. *Adv. Funct. Mater.* **2021**, *32*, 2110209. [[CrossRef](#)]
18. Yang, F.; Huang, Y.; Li, Y.; Li, Y. Large-area flexible organic solar cells. *NPJ Flex. Electron.* **2021**, *5*, 30. [[CrossRef](#)]
19. Kini, G.P.; Jeon, S.J.; Moon, D.K. Latest progress on photoabsorbent materials for multifunctional semitransparent organic solar cells. *Adv. Funct. Mater.* **2021**, *31*, 2007931. [[CrossRef](#)]
20. Brus, V.V.; Lee, J.; Luginbuhl, B.R.; Ko, S.J.; Bazan, G.C.; Nguyen, T.Q. Solution-processed semitransparent organic photovoltaics: From molecular design to device performance. *Adv. Mater.* **2019**, *31*, 1900904. [[CrossRef](#)] [[PubMed](#)]
21. Chen, W.; Zhang, J.; Xu, G.; Xue, R.; Li, Y.; Zhou, Y.; Hou, J.; Li, Y. A semitransparent inorganic perovskite film for overcoming ultraviolet light instability of organic solar cells and achieving 14.03% efficiency. *Adv. Mater.* **2018**, *30*, 1800855. [[CrossRef](#)]
22. Krebs, F.C. Fabrication and processing of polymer solar cells: A review of printing and coating techniques. *Sol. Energy Mater. Sol. Cells* **2009**, *93*, 394. [[CrossRef](#)]
23. Xue, P.; Cheng, P.; Han, R.P.S.; Zhan, X. Printing fabrication of large-area non-fullerene organic solar cells. *Mater. Horiz.* **2022**, *9*, 194. [[CrossRef](#)]
24. Wang, G.; Adil, M.A.; Zhang, J.; We, Z. Large-Area Organic Solar Cells: Material Requirements, Modular Designs, and Printing Methods. *Adv. Mater.* **2019**, *31*, 1805089. [[CrossRef](#)]
25. Ghosh, A.; Bhandari, S.; Sundaram, S.; Mallick, T.K. Carbon counter electrode mesoscopic ambient processed & characterised perovskite for adaptive BIPV fenestration. *Renew. Energy* **2020**, *145*, 2151. [[CrossRef](#)]
26. Cannavale, A.; Ierardi, L.; Hörantner, M.; Eperon, G.E.; Snaith, H.J.; Ayr, U.; Martellotta, F. Improving energy and visual performance in offices using building integrated perovskite-based solar cells: A case study in Southern Italy. *Appl. Energy* **2017**, *205*, 834. [[CrossRef](#)]
27. Cannavale, A.; Hörantner, M.; Eperon, G.E.; Snaith, H.J.; Fiorito, F.; Ayr, U.; Martellotta, F. Building integration of semitransparent perovskite-based solar cells: Energy performance and visual comfort assessment. *Appl. Energy* **2017**, *194*, 94–107. [[CrossRef](#)]
28. Xu, J.; Chen, Y.; Dai, L. Efficiently photo-charging lithium-ion battery by perovskite solar cell. *Nat. Commun.* **2015**, *6*, 8103. [[CrossRef](#)]
29. Kaltenbrunner, M.; White, M.S.; Glowacki, E.D.; Sekitani, T.; Someya, T.; Sariciftci, N.S.; Bauer, S. Ultrathin and lightweight organic solar cells with high flexibility. *Nat. Commun.* **2012**, *3*, 770. [[CrossRef](#)]
30. Güler, E.N.; Distler, A.; Basu, R.; Brabec, C.J.; Egelhaaf, E.-J. Fully solution-processed, light-weight, and ultraflexible organic solar cells. *Flex. Print. Electron.* **2022**, *7*, 025003. [[CrossRef](#)]

31. Chen, X.; Xu, G.; Zeng, G.; Gu, H.; Chen, H.; Xu, H.; Yao, H.; Li, Y.; Hou, J.; Li, Y. Realizing ultrahigh mechanical flexibility and >15% efficiency of flexible organic solar cells via a “welding” flexible transparent electrode. *Adv. Mater.* **2020**, *32*, 1908478. [[CrossRef](#)]
32. Li, S.; Li, Z.; Wan, X.; Chen, Y. Recent progress in flexible organic solar cells. *eScience* **2022**, *3*, 100085. [[CrossRef](#)]
33. Li, X.; Xia, R.; Yan, K.; Ren, J.; Yip, H.-L.; Li, C.-Z.; Chen, H. Semitransparent organic solar cells with vivid colors. *ACS Energy Lett.* **2020**, *5*, 3115. [[CrossRef](#)]
34. Jeong, E.G.; Jeon, Y.; Cho, S.H.; Choi, K.C. Textile-based washable polymer solar cells for optoelectronic modules: Toward self-powered smart clothing. *Energy Environ. Sci.* **2019**, *12*, 1878. [[CrossRef](#)]
35. Hashemi, S.A.; Ramakrishna, S.; Aberle, A.G. Recent progress in flexible–wearable solar cells for self-powered electronic devices. *Energy Environ. Sci.* **2020**, *13*, 685. [[CrossRef](#)]
36. Lv, D.; Jiang, Q.; Shang, Y. Highly efficient fiber-shaped organic solar cells toward wearable flexible electronics. *NPJ Flex. Electron.* **2022**, *6*, 38. [[CrossRef](#)]
37. Nicolaidis, N.C.; Hollott, P.V.; Stanwell, B.; Gill, I.A.; Bull, J.E.; Bentsen, S.; Iredale, J.; Pappenfus, T.M.; Dastoor, P.C.; Feron, K.; et al. Developing a Portable Organic Solar Cell Kit Suitable for Students to Fabricate and Test Solar Cells in the Laboratory. *J. Chem. Educ.* **2020**, *97*, 3751. [[CrossRef](#)]
38. Jahandar, M.; Kim, S.; Lim, D.C. Indoor organic photovoltaics for self-sustaining IoT devices: Progress, challenges and practicalization. *ChemSusChem* **2021**, *14*, 3449–3474. [[CrossRef](#)]
39. Hwang, S.; Yasuda, T. Indoor photovoltaic energy harvesting based on semiconducting  $\pi$ -conjugated polymers and oligomeric materials toward future IoT applications. *Polym. J.* **2023**, *55*, 297–316. [[CrossRef](#)]
40. Arai, R.; Furukawa, S.; Hidaka, Y.; Komiyama, H.; Yasuda, T. High-performance organic energy-harvesting devices and modules for self-sustainable power generation under ambient indoor lighting environments. *ACS Appl. Mater. Interfaces* **2019**, *11*, 9259. [[CrossRef](#)]
41. Luke, J.; Corrêa, L.; Rodrigues, J.; Martins, J.; Daboczi, M.; Bagnis, D.; Kim, J.-S. A Commercial Benchmark: Light-Soaking Free, Fully Scalable, Large-Area Organic Solar Cells for Low-Light Applications. *Adv. Energy Mater.* **2021**, *11*, 2003405. [[CrossRef](#)]
42. Nandy, S.; Fortunato, E.; Martins, R. Green economy and waste management: An inevitable plan for materials science. *Prog. Nat. Sci. Mater. Int.* **2022**, *32*, 1–9. [[CrossRef](#)]
43. Nandy, S.; Goswami, S.; Marques, A.; Gaspar, D.; Grey, P.; Cunha, I.; Nunes, D.; Pimentel, A.; Igreja, R.; Barquinha, P.; et al. Cellulose: A contribution for the zero e-waste challenge. *Adv. Mater. Technol.* **2021**, *6*, 2000994. [[CrossRef](#)]
44. Takada, T.; Uchiyama, T.; Okada-Shudo, Y.; Hoshino, K.; Koizumi, K.; Takeoka, Y.; Vohra, V. High performance organic solar cells fabricated using recycled transparent conductive substrates. *ACS Sustain. Chem. Eng.* **2020**, *8*, 5807–5814. [[CrossRef](#)]
45. Zhou, Y.; Fuentes-Hernandez, C.; Khan, T.M.; Liu, J.-C.; Hsu, J.; Shim, J.W.; Dindar, A.; Youngblood, J.P.; Moon, R.J.; Kippelen, B. Recyclable organic solar cells on cellulose nanocrystal substrates. *Sci. Rep.* **2013**, *3*, 1536. [[CrossRef](#)]
46. Rasool, S.; Yeop, J.; Cho, H.W.; Lee, W.; Kim, J.W.; Yuk, D.; Kim, J.Y. Path to the fabrication of efficient, stable and commercially viable large-area organic solar cells. *Mater. Future* **2023**, *2*, 031202. [[CrossRef](#)]
47. Lee, H.K.H.; Wu, J.; Barbé, J.; Jain, S.M.; Wood, S.; Speller, E.M.; Li, Z.; Castro, F.A.; Durrant, J.R.; Tsoi, W.C. Organic photovoltaic cells-promising indoor light harvesters for self-sustainable electronics. *J. Mater. Chem. A* **2018**, *6*, 5618. [[CrossRef](#)]
48. Burlingame, Q.; Song, B.; Ciannaruchi, L.; Zanotti, G.; Hankett, J.; Chen, Z.; Katz, E.A.; Forrest, S.R. Reliability of Small Molecule Organic Photovoltaics with Electron-Filtering Compound Buffer Layers. *Adv. Energy Mater.* **2016**, *6*, 1601094. [[CrossRef](#)]
49. Peters, C.H.; Sachs-Quintana, I.-T.; Kastrop, J.P.; Beaupré, S.; Leclerc, M.; McGehee, M.D. High efficiency polymer solar cells with long operating lifetimes. *Adv. Energy Mater.* **2011**, *1*, 491. [[CrossRef](#)]
50. Du, X.; Heumueller, T.; Gruber, W.; Classen, A.; Unruh, T.; Li, N.; Brabec, C.J. Efficient Polymer Solar Cells Based on Non-fullerene Acceptors with Potential Device Lifetime Approaching 10 Years. *Joule* **2019**, *3*, 215. [[CrossRef](#)]
51. Burlingame, Q.; Huang, X.; Liu, X.; Forrest, S.R. Intrinsically stable organic solar cells under high-intensity illumination. *Nature* **2019**, *573*, 394. [[CrossRef](#)] [[PubMed](#)]
52. Kawano, K.; Pacios, R.; Poplavskyy, D.; Nelson, J.; Bradley, D.D.C.; Durrant, J.R. Degradation of organic solar cells due to air exposure. *Sol. Energy Mater. Sol. Cells* **2006**, *20*, 3520. [[CrossRef](#)]
53. Wang, X.; Zhao, C.X.; Xu, G.; Chen, Z.-K.; Zhu, F. Degradation mechanisms in organic solar cells: Localized moisture encroachment and cathode reaction. *Sol. Energy Sol. Cells* **2012**, *104*, 1–6. [[CrossRef](#)]
54. Ye, L.; Hu, H.; Ghasemi, M.; Wang, T.; Collins, B.A.; Kim, J.-H.; Jiang, K.; Carpenter, J.H.; Li, H.; Li, Z.; et al. Quantitative relations between interaction parameter, miscibility and function in organic solar cells. *Nat. Mater.* **2018**, *17*, 253–260. [[CrossRef](#)] [[PubMed](#)]
55. Jørgensen, M.; Norrman, K.; Krebs, F.C. Stability/degradation of polymer solar cells. *Sol. Energy Mater. Sol. Cells* **2008**, *92*, 686. [[CrossRef](#)]
56. Pacios, R.; Chatten, A.J.; Kawano, K.; Durrant, J.R.; Bradley, D.D.C.; Nelson, J. Effects of Photo-oxidation on the Performance of Poly[2-methoxy-5-(3',7'-dimethyloctyloxy)-1,4-phenylene vinylene]:[6,6]-Phenyl C61-Butyric Acid Methyl Ester Solar Cells. *Adv. Funct. Mater.* **2006**, *16*, 2117. [[CrossRef](#)]
57. Howard, I.A.; Mauer, R.; Meister, M.; Laquai, F. Effect of Morphology on Ultrafast Free Carrier Generation in Polythiophene:Fullerene Organic Solar Cells. *J. Am. Chem. Soc.* **2010**, *132*, 14866. [[CrossRef](#)]
58. Xiao, Z.; Yuan, Y.; Yang, B.; VanDerslice, J.; Chen, J.; Dyck, O.; Duscher, G.; Huang, J. Universal formation of compositionally graded bulk heterojunction for efficiency enhancement in organic photovoltaics. *Adv. Mater.* **2014**, *26*, 3068. [[CrossRef](#)]

59. Meng, B.; Wang, Z.; Ma, W.; Xie, Z.; Liu, J.; Wang, L. A Cross-Linkable Donor Polymer as the Underlying Layer to Tune the Active Layer Morphology of Polymer Solar Cells. *Adv. Funct. Mater.* **2016**, *26*, 226. [[CrossRef](#)]
60. He, Z.; Xiao, B.; Liu, F.; Wu, H.; Yang, Y.; Xiao, S.; Wang, C.; Russell, T.P.; Cao, Y. Single-junction polymer solar cells with high efficiency and photovoltage. *Nat. Photon.* **2015**, *9*, 174. [[CrossRef](#)]
61. Song, S.; Kranthiraja, K.; Heo, J.; Kim, T.; Walker, B.; Jin, S.-H.; Kim, J.Y. Efficiency exceeding 11% in tandem polymer solar cells employing high open-circuit voltage wide-bandgap  $\pi$ -conjugated polymers. *Adv. Energy Mater.* **2017**, *7*, 1700782. [[CrossRef](#)]
62. He, Z.; Zhong, C.; Su, S.; Xu, M.; Wu, H.; Cao, Y. Enhanced power-conversion efficiency in polymer solar cells using an inverted device structure. *Nat. Photon.* **2012**, *6*, 591. [[CrossRef](#)]
63. Lee, C.-Y.; Tsao, C.-S.; Lin, H.-K.; Cha, H.-C.; Chung, T.-Y.; Sung, Y.-M.; Huang, Y.-C. Encapsulation improvement and stability of ambient roll-to-roll slot-die-coated organic photovoltaic modules. *Sol. Energy* **2021**, *213*, 136. [[CrossRef](#)]
64. Chen, J.; Yu, X.; Hong, K.; Messman, J.M.; Pickel, D.L.; Xiao, K.; Dadmun, M.D.; Mays, J.W.; Rondinone, A.J.; Sumpterand, B.G.; et al. Ternary Behavior and Systematic Nanoscale Manipulation of Domain Structures in P3HT/PCBM/P3HT-b-PEO Films. *J. Mater. Chem.* **2012**, *22*, 13013. [[CrossRef](#)]
65. Chen, H.P.; Chen, J.H.; Yin, W.; Yu, X.; Shao, M.; Xiao, K.; Hong, K.L.; Pickel, D.L.; Kochemba, W.M.; Kilbey II, S.M.; et al. Correlation of Polymeric Compatibilizer Structure to its Impact on the Morphology and Function of P3HT:PCBM Bulk Heterojunctions. *J. Mater. Chem. A* **2013**, *1*, 5309. [[CrossRef](#)]
66. Cheng, P.; Zhan, X. Versatile Third Components for Efficient and Stable Organic Solar Cells. *Mater. Horiz.* **2015**, *2*, 462. [[CrossRef](#)]
67. An, Q.; Zhang, F.; Zhang, J.; Tang, W.; Deng, Z.; Hu, B. Versatile Ternary Organic Solar Cells: A Critical Review. *Energy Environ. Sci.* **2016**, *9*, 281. [[CrossRef](#)]
68. Balis, N.; Verykios, A.; Soultati, A.; Constantoudis, V.; Papadakis, M.; Kournoutas, F.; Drivas, C.; Skoulikidou, M.-C.; Gardelis, S.; Fakis, M.; et al. Triazine-substituted zinc porphyrin as an electron transport interfacial material for efficiency enhancement and degradation retardation in planar perovskite solar cells. *ACS Appl. Energy Mater.* **2018**, *1*, 3216. [[CrossRef](#)]
69. Tountas, M.; Verykios, A.; Polydorou, E.; Kaltzoglou, A.; Soultati, A.; Balis, N.; Angaridis, P.A.; Papadakis, M.; Nikolaou, V.; Auras, F.; et al. Engineering of porphyrin molecules for use as effective cathode interfacial modifiers in organic solar cells of enhanced efficiency and stability. *ACS Appl. Mater. Interfaces* **2018**, *10*, 20728. [[CrossRef](#)]
70. Piradi, V.; Xu, X.; Wang, Z.; Ali, J.; Peng, Q.; Liu, F.; Zhu, X. Panchromatic ternary organic solar cells with porphyrin dimer and absorption-complementary benzodithiophene-based small molecules. *ACS Appl. Mater. Interfaces* **2019**, *11*, 6283–6291. [[CrossRef](#)]
71. Kadish, K.M.; Boisselier-Cocolios, B.; Coutsolelos, A.; Mitaine, P.; Guillard, R. Electrochemistry and Spectroelectrochemistry of Gallium(III) Porphyrins. Redox properties of Five-Coordinate Ionic and Sigma-Bonded Complexes. *Inorg. Chem* **1985**, *24*, 4521–4528. [[CrossRef](#)]
72. Coutsolelos, A.; Guillard, R. Synthèse et caractéristiques physicochimiques de gallioporphyrynes à liaison  $\sigma$  métal carbone. *J. Organomet. Chem.* **1983**, *253*, 273–282. [[CrossRef](#)]
73. Coutsolelos, A.; Guillard, R.; Bayeul, D.; Lecomte, C. Gallium (III) porphyrins: Synthesis and physicochemical characteristics of halogeno gallium (III) porphyrins-X-ray crystal structure of chloro-(5,10,15,20-tetraphenylporphyrinato) gallium (III). *Polyhedron* **1986**, *5*, 1157–1164. [[CrossRef](#)]
74. Cardona, C.M.; Li, W.; Kaifer, A.E.; Stockdale, D.; Bazan, G.C. Electrochemical considerations for determining absolute frontier orbital energy levels of conjugated polymers for solar cell applications. *Adv. Mater.* **2011**, *23*, 2367–2371. [[CrossRef](#)]
75. Panigrahi, S.; Jana, S.; Calmeiro, T.; Nunues, D.; Deurmeier, J.; Martins, R.; Fortunato, E. Mapping the space charge carrier dynamics in plasmon-based perovskite solar cells. *J. Mater. Chem. A* **2019**, *7*, 19811–19819. [[CrossRef](#)]
76. Mendes, M.J.; Araujo, A.; Vicente, A.; Aguas, H.; Ferreira, I.; Fortunato, E.; Martins, R. Design of optimized wave-optical spheroidal nanostructures for photonic-enhanced solar cells. *Nano Energy* **2016**, *26*, 286–296. [[CrossRef](#)]
77. Saito, M.; Yamada, H.; Kranthiraja, K.; Mikie, T.; Saeki, A.; Ohkita, H.; Osaka, I. Ordered  $\pi$ -conjugated backbone in amorphous blend for high efficiency nonfullerene organic photovoltaics. *Commun. Mater.* **2023**, *4*, 72. [[CrossRef](#)]
78. Saito, M.; Ogawa, S.; Osaka, I. Contrasting effect of side-chain placement on photovoltaic performance of binary and ternary blend organic solar cells in benzodithiophene-thiazolothiazole polymers. *ChemSusChem* **2021**, *14*, 5032–5041. [[CrossRef](#)]
79. Honda, S.; Ohkita, H.; Benten, H.; Ito, S. Selective dye loading at the heterojunction in polymer/fullerene solar cells. *Adv. Energy Mater.* **2011**, *1*, 588–598. [[CrossRef](#)]
80. Kranthiraja, K.; Aryali, U.K.; Sree, V.G.; Gunasekar, K.; Lee, C.; Kim, M.; Kim, B.J.; Song, M.; Jin, S.-H. Efficient approach for improving the performance of nonhalogenated green solvent-processed polymer solar cells via ternary-blend strategy. *ACS Appl. Mater. Interfaces* **2018**, *10*, 13748–13756. [[CrossRef](#)]
81. Li, D.; Zeng, Y.; Chen, Z.; Leng, S.; Xiao, Z.; Xue, Q.; Hao, T.; Lv, M.; Wu, H.; Lin, L. Investigating the reason for high FF from ternary organic solar cells. *J. Semicond.* **2021**, *42*, 090501. [[CrossRef](#)]

**Disclaimer/Publisher's Note:** The statements, opinions and data contained in all publications are solely those of the individual author(s) and contributor(s) and not of MDPI and/or the editor(s). MDPI and/or the editor(s) disclaim responsibility for any injury to people or property resulting from any ideas, methods, instructions or products referred to in the content.